ACS Catalysis

Research Article

pubs.acs.org/acscatalysis

Shaping Single-Crystalline Trimetallic Pt–Pd–Rh Nanocrystals toward High-Efficiency C–C Splitting of Ethanol in Conversion to CO_2

Wei Zhu,[†,‡] Jun Ke,[†,‡] Si-Bo Wang,[†] Jie Ren,[§] Hong-Hui Wang,[§] Zhi-You Zhou,*[,§] Rui Si,[⊥] Ya-Wen Zhang,*[,†] and Chun-Hua Yan*[,†]

[†]Beijing National Laboratory for Molecular Sciences, State Key Laboratory of Rare Earth Materials Chemistry and Applications, PKU-HKU Joint Laboratory in Rare Earth Materials and Bioinorganic Chemistry, College of Chemistry and Molecular Engineering, Peking University, Beijing 100871, China

[§]State Key Laboratory of Physical Chemistry of Solid Surfaces, Department of Chemistry, College of Chemistry and Chemical Engineering, Xiamen University, Xiamen 361005, China

[⊥]Shanghai Synchrotron Radiation Facility, Shanghai Institute of Applied Physics, Chinese Academy of Sciences, Shanghai 201204, China

Supporting Information

ABSTRACT: Atomic-scale construction and high-throughput screening of robust multicomponent nanocatalysts with tunable well-defined surface structures and associated active sites for the ethanol electro-oxidation reaction (EOR) in high activity and selectivity, referring to C–C bond cleavage and full oxidation of ethanol as a clean and sustainable energy source, has remained a great challenge. Herein, we demonstrate a powerful conceptual approach to design, synthesize, and optimize single-crystalline Pt–Pd–Rh nanocrystals of altered shapes and compositions for enhanced EOR performance, based on combined density functional theory (DFT) calculations and experiment study. We prepared (111)-terminated Pt–Pd–Rh nanotruncated-octahedrons (NTOs) and (100)-terminated Pt–Pd–Rh nanocubes (NCs) with varied-compositions by regulating the reduction tendency of metal precursors in a facile hydrothermal method. Aided by DFT calculations, Pt_3PdRh NTOs, PtPdRh NTO, and 8.8 nm PtPdRh NCs-200 were screened to be the best performing catalysts with the highest EOR activity (five times as much as that of commercial Pt black) at 0.5 V vs NHE. Among these catalysts, PtPdRh NTOs exhibited the highest selectivity to CO_2 at 0.5 V and the noteworthy capability to fully oxidize ethanol at extremely low potential (0.35 V); 8.8 nm PtPdRh NCs-200 possessed the best durability. Morphology and surface composition correlated to the synergistic effect of three metals were verified to affect the EOR performance of well-shaped Pt–Pd–Rh nanocrystals. Combined with in situ FTIR, it was deduced that appropriate surface composition and exposed facets were the key factors to the promoted capability in the cleavage of C–C bond down to low potential. Through adjusting surface composition and morphology of Pt–Pd–Rh nanocrystals with homogeneous element distribution, enhanced EOR performance was achieved in light of DFT simulations of the two elementary reactions (i.e., breakdown of C–C bond and oxidation of CO_{ad}). This work has offered an effective and useful strategy to promote the reactivity of multicomponent heterogeneous nanocatalysts with optimized compositions and surface structures for many industrial catalytic processes.

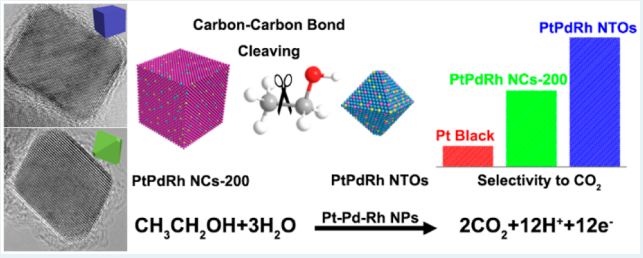

KEYWORDS: *trimetallic Pt–Pd–Rh nanocrystals, ethanol electro-oxidation reaction, controllable syntheses, in situ FTIR, C–C bond splitting, DFT calculations*

1. INTRODUCTION

Of both scientific and technological importance, the development of novel high-performance (active, selective, and durable) inorganic nanocatalysts plays a central role in enhancing and maximizing the conversion efficiency of renewable energy resources of biomasses such as ethanol biofuel and biodiesel.[1−3] Ethanol, a hydrogen-rich liquid fuel with high energy density (8.0 kWh/kg), acts as an attractive alternative for current fuels (e.g., gasoline, methanol, etc.) due to its low toxicity and abundant sources from biomass. Direct ethanol fuel cells (DEFCs), which are applied for the efficient and eco-friendly utilization of ethanol, have the advantages in the facile storage of fuels and relative low operation temperature, and have received extensive attentions in the most recent years.[4−7] Nevertheless, sluggish kinetics reactions of anode reactions (ethanol electro-oxidation reaction, EOR), especially the inferior performance of catalysts, are the main issue which retards the development of DEFCs. Unlike methanol electro-

Received: November 20, 2014
Revised: January 21, 2015
Published: February 16, 2015

DOI: 10.1021/cs5018419
ACS Catal. 2015, 5, 1995−2008

oxidation reaction (MOR), EOR is restricted by a partial oxidation path with the formation of C2 species (i.e., acetic acid, acetaldehyde) in high yield, rather than the poisoning of adsorbed CO (CO_{ad}), leading to the low energy utilization of ethanol.[8−13] Promoting the ability to fully oxidize ethanol into CO_2 (i.e., dissociation of C−C bond) is the major aim for the current EOR catalysts.

Due to the incompetence of single and binary metal catalysts for EOR which constituted of complicated substep reactions (e.g., dehydrogenation, breakdown of C−C bond, oxidation of CO_{ad}), construction of multicomponent catalysts to create multiply catalytic sites is a promising route to improve the activity of the catalysts by bifunctional effect and electronic interplay from various constituents. As the primary component of EOR catalysts, Pt has strong capabilities in ethanol dehydrogenation and CO_{ad} oxidation, while suffering the difficulty in the breakdown of C−C bond. The Rh component is manifested to be beneficial to the cleavage of C−C bond in EOR.[14,15] Pt−Rh catalysts can improve the selectivity to CO_2, but usually act at a low overall activity due to the Rh−CO contaminants and the limited dehydrogenation rate.[16] By introducing components that facilitate the formation of hydroxyl groups, Adzic's group has developed multicomponent $PtRh/SnO_2$ and $PtRhIr/SnO_2$ catalysts for EOR with improved catalytic performance.[17−19] Besides supported ternary catalysts, trimetallic nanoparticles are applied to improve EOR performance because of abundant intraparticle active interfacial sites and tunable d-band position. Many groups have reported the enhanced EOR activity of Pt−Ru- and Pt−Sn-based multimetallic nanocatalysts by facilitating the oxidation of CO_{ad}, whereas the finite improvement is restricted by the cleavage of C−C bond.[20−22] Also several multimetallic nanocatalysts suffered the deactivation by blocking the Pt sites with formation of metal oxides.[23] More recently incorporation of a third metal into PtSn/C was revealed to be a feasible strategy to facilitate the cleavage of C−C bond and reactivity toward the electrooxidation of C2 organics (e.g., ethanol, acetaldehyde, etc.) due to the enhanced strong Pt-carbon interaction.[24−27] It thus demands for an integration of stable active components for both of C−C bond cleaving and CO_{ad} oxidation in the design of multimetallic catalysts.[28] Here, trimetallic Pt−Pd−Rh nanostructure is proposed to be a promising candidate for efficient EOR catalysts, as Rh and Pd facilitates the breakdown of C−C bond and oxidation of CO_{ad} species,[17,29] respectively.

Controlled syntheses through various facile wet chemistry methods is an essential way to obtain multicomponent nanomaterials with the optimal catalytic performances.[30−33] Construction of nanoparticles with well-defined morphology and tunable surface (e.g., composition, strain, element distribution) helps to design the composite nanocatalysts and to rationalize the possible relations between structure and catalytic property.[34−38] However, controllable one-pot synthesis and surface modulation on structure as well as composition remains a challenge for ternary metallic alloys because of the appreciable differences in the redox potentials of various metal precursors. More recently, only limited examples dealt with shaped ternary metal nanocrystals (e.g., Au@Pd@Pt,[30] Pt-on-(Au@Pd),[31] FePtM (M = Cu, Ni),[32] Pt_3Ni@M (M = Au, Ag, Cu, Rh)[33]) with enhanced activity for MOR, EOR, oxygen reduction reaction, and the Suzuki−Miyaura reaction, which were mainly fabricated via seed-mediated methods in solutions, and mostly possessed core−shell structures.[30−33]

To optimize EOR catalysts with proper shape and composition, theoretical simulations have also been carried out for the exploration of structure−activity relationship and catalyst design based on catalytic mechanism study. Density functional theory (DFT) calculation is an efficient methodology in identification of reaction path, indication of intrinsic reaction mechanism, and catalyst design for high reactivity, as reported on $PtRh/SnO_2$, (111)-exposed Rh, RtRu, and other materials.[17,39−41] For ternary nanocatalysts with tunable compositions and morphologies, it is a large quantity of work not only for experiments but also for DFT calculations to select the optimal catalyst. A combination of experimental analysis and DFT calculations notably should be expected to reduce the workload in such a multivariate research system with high complexity, and this combination offers a prompt approach to select efficient catalysts as well as to understand the reaction mechanism.

In this article, for the first time, we report composition-varied trimetallic Pt−Pd−Rh nanocubes (NCs) and nanotruncated-octahedrons (NTOs) prepared via a one-pot hydrothermal method with enhanced EOR activity and selectivity. DFT simulation based on experimentation concurrently guided the shape and composition optimization of the trimetallic nanocatalysts toward EOR. With combined DFT calculation and experiments, surface composition and exposed facets were revealed as the key factors for promoting the capability in the breakdown of C−C bond in EOR. A simple criterion to screen optimal Pt−Pd−Rh catalysts was established.

2. EXPERIMENTAL SECTION

2.1. Chemicals. $RhCl_3·3H_2O$ (A.R.; Sinopharm Chemical Reagent Co., Ltd., China), H_2PtCl_6 (A.R.; Shenyang Institute of Nonferrous Metal, China), $PdCl_2$ (A.R.; Shenyang Institute of Nonferrous Metal, China), Na_2PdCl_4 (prepared by mixing 2 equiv of NaCl and 1 equiv of $PdCl_2$ with string overnight.), KI (A.R.; Beijing Chemical Works, China), HCl (A.R.; Beijing Chemical Works, China), KBr (A.R.; Beijing Chemical Works, China), poly(vinylpyrrolidone) (PVP; M.W.: ∼29 000; Sigma-Aldrich), tin(II) chloride dihydrate (A.R.; Xilong Chemical Co., Ltd., China), $Sn(acac)_2$ (acac = acetyl-acetonate) (>98%; STREM), $Pt(acac)_2$ (Pt 48.0% min; Alfa Aesar), $Rh(acac)_3$ (97%; Aldrich), 1,2-tetradecanediol (90%; TCI), 1-octadecene (>90%; J&K Chemical Ltd.), oleic acid (>90%; Aldrich), oleylamine (>80%; Acros), cyclohexane (A.R.; Beijing Chemical Works, China), $HClO_4$ (70%; Tianjin Xinyuan Chemical Co., Ltd.), Pt black (High surface area; Alfa Aesar), acetone (A.R.), ethanol (A.R.), deionized water (Millipore, 18.2 MΩ·cm).

2.2. Synthesis of Bimetallic or Trimetallic NPs. *Synthesis of Trimetallic Pt−Pd−Rh NCs.* In a typical synthesis of Pt−Pd−Rh NCs with various compositions, 0.06 mmol of total metal precursors ($RhCl_3$, H_2PtCl_6, and Na_2PdCl_4), certain amounts of KBr and KI, 0.05 mmol of HCl (1.0 $mol·L^{-1}$), and 100 mg of PVP were dissolved in 15 mL of deionized water with stirring for 10 min. The solution was transferred to a 25 mL Teflon-lined stainless steel autoclave and heated at 180 °C for 4 h. After the mixture was cooled, the black products were centrifuged with the introduction of 40 mL of acetone and washed by water/acetone and ethanol/acetone several times. To obtain NCs with a Pt/Pd/Rh molar ratio of 1:1:1 (PtPdRh NCs for short), 0.02 mmol of H_2PtCl_6, 0.02 mmol of Na_2PdCl_4, 0.02 mmol of $RhCl_3$, 6 mmol of KBr, and 1 mg of KI were added; to obtain NCs with a Pt/Pd/Rh molar ratio of 3:1:1

DOI: 10.1021/cs5018419
ACS Catal. 2015, 5, 1995−2008

(Pt_3PdRh NCs for short), 0.036 mmol of H_2PtCl_6, 0.012 mmol of Na_2PdCl_4, 0.012 mmol of $RhCl_3$, 6 mmol of KBr, and 1 mg of KI were added.

Synthesis of Trimetallic Pt−Pd−Rh NTOs. The synthesis of Pt−Pd−Rh NTOs is similar to that of Pt−Pd−Rh NCs, except for the absence of KI and the increased reaction time to 12 h. To obtain Pt−Pd−Rh NTOs with a 1:1:1 Pt/Pd/Rh ratio in precursors (PtPdRh NTOs for short), 0.02 mmol of H_2PtCl_6, 0.02 mmol of Na_2PdCl_4, 0.02 mmol of $RhCl_3$, and 6 mmol of KBr were added. To obtain Pt−Pd−Rh NTOs with a 3:1:1 Pt/Pd/Rh ratio in precursors (Pt_3PdRh NTOs for short), 0.036 mmol of H_2PtCl_6, 0.012 mmol of Na_2PdCl_4, 0.012 mmol of $RhCl_3$, and 3 mmol of KBr were added. To obtain Pt−Pd−Rh NTOs with a 1:3:1 Pt/Pd/Rh ratio in precursors ($PtPd_3Rh$ NTOs for short), 0.012 mmol of H_2PtCl_6, 0.036 mmol of Na_2PdCl_4, 0.012 mmol of $RhCl_3$, and 3 mmol of KBr were added.

Synthesis of Trimetallic Pt−Pd−Rh NCs with Homogeneous Element Distribution. The key point to obtain Pt−Pd−Rh NCs with homogeneous element distribution was to elevate the reaction temperature and level the oxidation capability of different metal ions. The synthetic method of Pt−Pd−Rh NCs with homogeneous element distribution (PtPdRh NCs-200) was the same as the synthesis of PtPdRh NCs, except that the reaction temperature was increased to 200 °C. By adjusting the addition amount of KI and KBr, Pt−Pd−Rh NCs-200 NCs with various sizes were obtained. For 8.8 nm PtPdRh NCs-200, 3 mmol of KBr and 1 mg of KI were added; for 13.8 nm PtPdRh NCs-200, 6 mmol of KBr and 2 mg of KI were added; For 18.5 nm PtPdRh NCs-200, 6 mmol of KBr and 1 mg of KI were added.

Synthesis of Bimetallic Pt−Pd and Pt−Rh NCs. Similar hydrothermal synthesis was performed except for the reaction temperature and the amounts of metal precursors, KBr, and KI. For Pt−Pd NCs, 0.03 mmol of K_2PtCl_4, 0.03 mmol of Na_2PdCl_4, 3.0 mmol of KBr, and 1 mg of KI were added, and the reaction was performed at 160 °C for 4 h as reported in our previous work.[42] For Pt−Rh NCs, 0.03 mmol of H_2PtCl_6, 0.03 mmol of $RhCl_3$, 6.0 mmol of KBr, and 1 mg of KI were added, and the reaction went on at 180 °C for 4 h.

Synthesis of PtRh(Sn)/SnO_2 NPs. Similar hydrothermal synthesis was conducted to synthesize PtRh(Sn)/SnO_2 NPs with an optimal Pt/Rh/Sn ratio of 3:1:4 as reported.[28] 0.06 mmol of H_2PtCl_6, 0.02 mmol of $RhCl_3$, 0.08 mmol of $SnCl_2$, 720 mg of KBr, 100 mg of PVP, and 0.05 mmol of HCl were mixed in deionized water with stirring and diluted to 15 mL. The solution was then transferred into a 25 mL Teflon-lined stainless steel autoclave and heated at 200 °C for 4 h. The as-obtained black products were centrifuged with the addition of 40 mL of acetone, washed by ethanol/acetone several times, and lastly dispersed in ethanol for the further characterizations.

Synthesis of Niggliite PtRhSn/C NPs. As referred to the published work, a similar method was applied in the fabrication of carbon supported niggliite PtRhSn NPs.[28] In the initial step, 118.1 mg of $Pt(acac)_2$, 40.7 mg of $Rh(acac)_3$, 129.7 mg of $Sn(acac)_2$, 207.1 mg of 1,2- tetradecanediol, 0.16 mL of oleic acid, 0.16 mL of oleylamine, and 20 mL of 1-octadecene were mixed in a three-neck flask and heated at 60 °C in vacuum. Then, the solution was heated up to 260 °C under N_2 gas flow and kept for half an hour. The as-obtained black colloidal solution was centrifuged with the addition of ethanol, washed by ethanol/cyclohexane, and dispersed in 50 mL of cyclohexane. All the colloidal cyclohexane solution was added into the cyclohexane solution which contained 100 mg of dispersed carbon black (VulcanXC-72) and treated under sonication for 1 h in ice water. After stirring overnight, the carbon-supported NPs were separated by centrifugation, dried under N_2 gas flow at 280 °C for 1 h, oxidized in air at 250 °C for 2 h, and calcinated under H_2 (10% in Ar) gas flow in furnace at 400 °C for 1 h.

2.3. Instrumentation. Transmission electron microscope (TEM), high-resolution transmission electron microscope (HRTEM), energy dispersive X-ray spectroscopy (EDS), and high-angle annular dark-field scanning transmission electron microscopy (HAADF-STEM) EDS line scan analysis were conducted on a FEG-TEM (JEM-2100F, JEOL, Japan) operated at 200 kV. The samples for TEM characterizations were prepared by dropping the colloid solution on copper grids coated with amorphous carbon and drying naturally. Powder X-ray diffraction (PXRD) analysis was performed on a Rigaku D/MAX-2000 diffractometer (Japan). Inductively coupled plasma-atomic emission spectroscopy (ICP-AES) analysis was conducted on a Profile Spec ICP-AES spectrometer (Leeman, U.S.A.). X-ray Photoelectron Spectroscopy (XPS) was carried out on an Axis Ultra Imaging Photoelectron Spectrometer (Kratos Analytical Ltd., U.K.) with a monochromatic Al Kα (1486.7 eV) X-ray source operated at 225 W with 15 kV acceleration voltage.

Pt L_3-edge, Pd K-edge, and Rh K-edge extended X-ray absorption fine structure (EXAFS) analysis was carried out both on the 1W2B beamline of Beijing Synchrotron Radiation Facility (BSRF) operated at 2.2 GeV with injection currents of 300−500 mA and on the BL14W1 beamline of Shanghai Synchrotron Radiation Facility (SSRF) operated at 3.5 GeV under "top-up" mode with current of 220 mA. Pt, Pd, and Rh foils were used as reference samples. All the spectra were collected in transmission mode. Athena and Artemis codes were used to extract the data and to fit the curves, respectively. The Fourier transformed curves were fitted in real space with Δk = 2.6−14.4 $Å^{-1}$ and ΔR = 1.3−3.3 Å (k^2 weighted).

2.4. First-Principles Calculations. DFT calculation was performed with the VASP code. Kohn−Sham equations were expanded into plain waves. The exchange-correlation energy functional was described in the Perdew−Burke−Ernzerhof generalized gradient approximation (GGA). In the Brillouin zone, the 5 × 5 × 1 Monkhorst−Pack special *k*-point mesh was automatically generated. The atoms were presented by projector augmented-wave (PAW) pseudopotentials. The kinetics energy cutoff for the plane-wave basis set was 400 eV. (100) and (111) surface exposed 3 × 3 × 6 metal supercells with three fixed layers and 15 Å of vacuum was built for the simulation. Pt, Pd, and Rh atoms were randomly placed with some varied composition and uniform distribution. Each structure was relaxed until the residual force was less than 0.02 eV/Å.

2.5. Preparation of Working Electrode and Removal of Capped PVP Surfactants. Ozone was generated from a 6 W low-pressure mercury lamp to remove the residual PVP on the surface of NPs, which was reported as a nondestructive method to remove surfactants on NPs.[43] First, 10 μL of the colloid NPs solution was dropped on a glassy carbon electrode and dried for preparing the working electrode. The sample on the electrode was positioned 5 mm from the lamp and radiated overnight. TEM image of UV/Ozone-treated PtPdRh NCs (Figure S1 in Supporting Information (SI)) confirmed it to be a nondestructive method to remove the surfactant on shaped

DOI: 10.1021/cs5018419
ACS Catal. 2015, 5, 1995−2008

nanoparticles. After the radiation, the samples on the working electrode were covered by 5 μL of 0.2 wt % Nafion (Sigma-Aldrich) solution and dried for further electrochemical measurements.

2.6. Electrochemical Measurements. Electrochemical measurements were conducted on a CHI 840B electrochemical analyzer (CH Instrument, TX, U.S.A.) in a standard three-electrode cell. In the three-electrode system, a glassy carbon (6 mm in diameter) electrode was used as the working electrode; a platinum foil was used as the counter electrode; a KCl-saturated Ag/AgCl electrode was used as the reference electrode. All the measurements were performed at room temperature, and the electrolyte used was freshly made. The electrochemically active surface area (ECSA) of each sample was calculated from the H-adsorption area ranging from 0 to 0.25 V (vs NHE) in the cathodic scan of CV measurement, which was carried out in 0.1 mol·L^{-1} $HClO_4$ aqueous solution at a sweep rate of 20 mV·s^{-1}, because the H-adsorption method has been applied in the measurement of ECSA of Pt, Pd, and Rh electrode previously.[44,45] The calculation equation of ECSA is

$$\mathrm{ECSA}\ (\mathrm{cm}^2) = Q_H/210\ \mu\mathrm{C}\cdot\mathrm{cm}^{-2} \quad (1)$$

The EOR property of each sample was evaluated by its quasi-steady polarization curve, which was obtained by linear sweep voltammetry in N_2-saturated 0.5 mol·L^{-1} CH_3CH_2OH/0.1 mol·L^{-1} $HClO_4$ aqueous solution at a sweep rate of 1 mV·s^{-1}. Before the evaluations of trimetallic nanocatalysts toward EOR, a hundred cycles of cyclic voltammetry ranged from 0 to 1.2 V at a sweep rate of 50 mV·s^{-1} were applied to remove the residues on surfaces. All the potentials used were normalized by normal hydrogen electrode (NHE).

2.7. In Situ Infrared Reflection Absorption Spectroscopy (FTIR). A Nicolet Nexus 870 Fourier transform infrared spectrometer equipped with a mercury cadmium telluride detector cooled with liquid nitrogen was employed in the in situ FTIR electrochemical study. A calcium fluoride window and an in situ EC-IR thin cell were applied in the test. The reference spectrum was collected at 0.05 V in 0.5 M CH_3CH_2OH/0.1 M $HClO_4$. Before the spectrum collection at each potential, the working electrode was cleaned at 1.2 V to remove the adsorbed species generated at the last potential, and then the voltage was switched to 0.05 V. Meanwhile, spectra under a continuous stepped potential were acquired. To subtract the signals from background, the spectrum at each potential was normalized by the reference spectrum as follows:[46]

$$\frac{\Delta R}{R}(E_S^i) = \frac{R(E_S^i) - R(E_R)}{R(E_R)} \quad (2)$$

$R(E_R)$ and $R(E_S^i)$ were the spectrum at reference potential and tested potential, respectively.

3. RESULTS AND DISCUSSION

3.1. Syntheses of Trimetallic Pt−Pd−Rh Nanocrystals. A facile one-pot hydrothermal method was applied in the controlled syntheses of Pt−Pd−Rh nanocrystals. (100)-Terminated Pt−Pd−Rh NCs were synthesized in a 4 h reaction with the addition of iodine and bromide (Figure 1a and Figure S2a in SI). In the presence of bromide, (111)-terminated Pt−Pd−Rh NTOs were obtained in the 12 h reaction (Figure 1b and Figure S2b in SI). In the syntheses, polyvinylpyrrolidone (PVP) served as the capping agent and

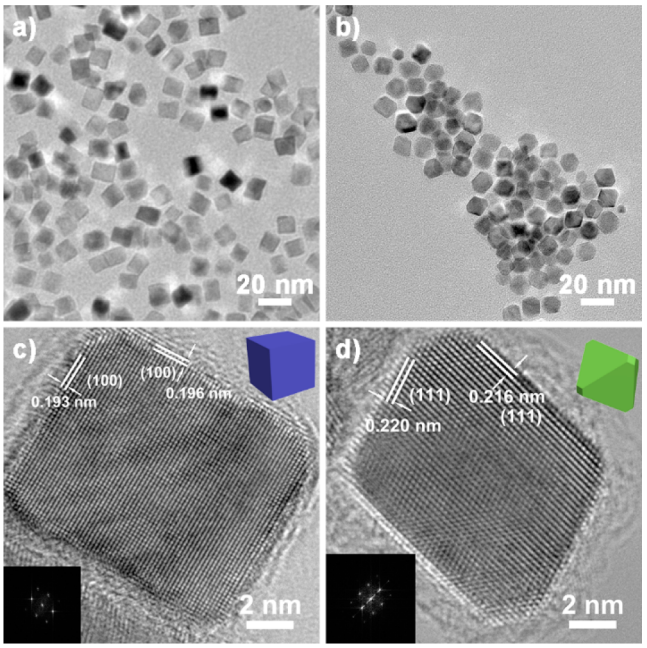

Figure 1. TEM images of (a) PtPdRh NCs and (b) PtPdRh NTOs; HRTEM images of (c) PtPdRh NCs and (d) PtPdRh NTOs. The insets in HRTEM images are the corresponding fast Fourier transform (FFT) patterns.

the reductant, with halide ions used for the construction of well-defined morphologies, as demonstrated by Figure S3.[47−50] With the fine adjustment of the facet-selective adsorption effects of bromide and iodine ions on the nanocrystal growth kinetics, the syntheses of composition-varied Pt−Pd−Rh NCs and NTOs in well-defined shapes could be realized through the synthetic strategy we developed (Figure S4 and S5 in SI).

3.2. Sampling by DFT Calculations. Before the further optimization on the synthesis condition for candidate Pt−Pd−Rh samples with varied compositions and well-defined shapes, a simplified DFT simulation was performed for the composition effect on EOR performance regardless of the influence of solvent environment, applied potential, coverage of adsorbents, and so on.[51] Considering the high complexity in enumerating the possible atomic arrangement of the ternary metal models, only two extreme cases were taken into account: unitary metal and highly mixed ternary ones with uniform atom distribution. To increase the screening efficiency further, for each Pt−Pd−Rh composition, only one randomly placed model was calculated. Although error might exist to a certain degree in each isolated structure, some trends might be revealed on the varied compositions. The calculation was performed on both (100) and (111) exposed models based the above synthetic experiments.

According to some current reports, high dissociation capability of C−C bond is the major target for our Pt−Pd−Rh catalysts design. For the breakdown of C−C bond, two reported pathways[17,41] have been suggested:

$$CH_2CH_2O_{(ad)} = CH_{2(ad)} + CH_2O_{(ad)} \quad (3)$$

$$CHCO_{(ad)} = CH_{(ad)} + CO_{(ad)} \quad (4)$$

Their corresponding breakdown energy was calculated as eq 5 and eq 6, respectively:

DOI: 10.1021/cs5018419
ACS Catal. 2015, 5, 1995−2008

$$\Delta E(\mathrm{I}) = E(\text{metal with } CH_2) + E(\text{metal with } CH_2O) - E(\text{metal with } CH_2CH_2O) - E(\text{metal}) \quad (5)$$

$$\Delta E(\mathrm{II}) = E(\text{metal with CH}) + E(\text{metal with CO}) - E(\text{metal with CHCO}) - E(\text{metal}) \quad (6)$$

The oxidation of CO_{ad} on Pt−Pd−Rh crystal planes was also taken into account (replacing H^+ (aq) with an isolated H atom would not change the variation sequence):

$$CO_{(ad)} + OH_{(ad)} = CO_{2(g)} + H^+_{(aq)} + e^- \quad (7)$$

$$\Delta E(\mathrm{III}) = E(\text{metal}) \times 2 + E(CO_2) + E(H) - E(\text{metal with CO}) - E(\text{metal with OH}) \quad (8)$$

To improve the total efficiency of the simulation prediction, only these two steps were chosen, simply because both of them were examined as the main obstacles in EOR from the reported experimental analysis.[52] The other steps (e.g., dehydrogenation, formation of hydroxyl, less important steps in EOR) were all ignored in the DFT screening. All the simulation results were listed in the triangular diagrams in Figure 2 and Table S1.

The results simulated by the two reaction paths for the breakdown of C−C bond illustrated that alloyed ternary catalysts were expected to exhibit a better reactivity in the cleavage of C−C bond than monometallic catalysts, indicating a synergistic effect among Pt, Pd, and Rh in the ternary catalysts to the full conversion reactions of ethanol (e.g., EOR, ethanol steam reforming, etc.). Reaction energies of monometallic planes also suggested the capability of Rh in cleavage of C−C bond and that of Pd in oxidation of CO_{ad}. For (100) planes, Pd-rich regions had low reaction energy for $CH_2CH_2O_{(ad)}$ decomposition (Figure 2a). Decomposition energy of $HCCO_{(ad)}$ on Pt−Pd−Rh alloy seemed to be similar, and no clear trend was found on the varied composition (Figure 2c). For composition-varied ternary (111) planes, the region from the Pt/Pd/Rh ratio of 1:1:1 to the Pd-rich one was expected to exhibit high reactivity in the decomposition of $CH_2CH_2O_{(ad)}$ (Figure 2b), and a similar trend could be found in the decomposition of $HCCO_{(ad)}$ (Figure 2d). Therefore, besides Pd-rich planes, ternary planes with the Pt/Pd/Rh molar ratio of 1:1:1, especially for (111), were projected to be efficient for the breakdown of C−C bond.

Furthermore, DFT simulations on CO_{ad} oxidation were also conducted on the random-alloyed PtPdRh (111) and (100) planes. OH_{ad} was regarded as the major oxidant in the electrochemical reactions. Consequently, removal of CO_{ad} was proposed to be accomplished with OH_{ad}, as illustrated in eq 7. For (100) planes, the reaction energy turned out to be quite close with the lowest values at the Pt/Pd/Rh ratios of 1:1:1 and 1:7:1 (Figure 2e). However, Pt-rich regions were favorable for CO oxidation on (111) planes (with the highest energy barrier at the Pt/Pd/Rh ratio of 1:1:1) (Figure 2f). It demonstrated that the increasing Pt component for Pt−Pd−Rh NTOs might enhance the capability of CO_{ad} oxidation, whereas the CO_{ad} oxidation capabilities over composition-varied Pt−Pd−Rh NCs were similar.

Due to incapability in the synthesis of well-defined Pd-rich NCs, PtPdRh NCs, Pt_3PdRh NCs, PtPdRh NTOs, Pt_3PdRh NTOs, and $PtPd_3Rh$ NTOs were selected as the typical model catalysts in experimental studies of EOR, with a focus on exposed facets, surface composition, and their EOR activities.

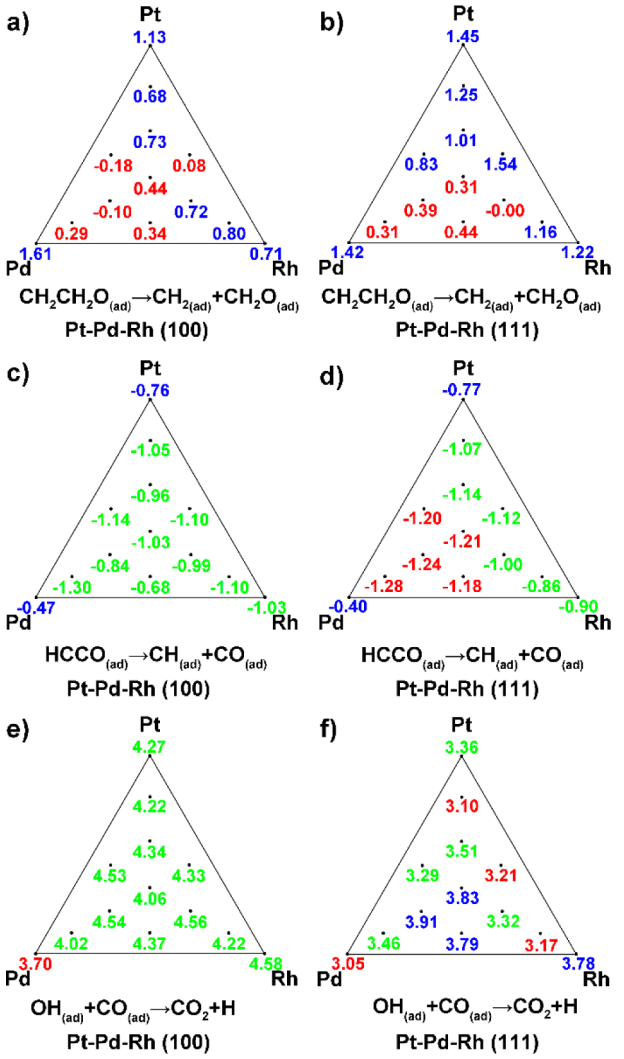

Figure 2. DFT calculations performed on random-alloyed Pt−Pd−Rh (111) and (100) planes with various compositions. The reaction energies for each composition were listed in the triangular diagrams with the subscript reaction path and crystal plane: the red ones represented favorable region with high expectations; the green ones were ordinary for the reactions; the blue ones were adverse.

3.3. Structure and Composition Characterization of Shaped Ternary Nanocrystals. As shown in Figure 1a and Figure S4a, Pt−Pd−Rh NCs with two different compositions were synthesized in high selectivity with the modulation of KBr and KI. The average sizes of PtPdRh NCs and Pt_3PdRh NCs were 12.0 ± 1.6 nm and 16.4 ± 2.0 nm, respectively. HRTEM images (Figure 1c, Figure S4b in SI) viewed along the ⟨001⟩ zone axis showed that the single-crystalline Pt−Pd−Rh NCs were enclosed with six (100) planes. From the lattice fringes, the distances of (100) planes were between 0.191 and 0.196 nm, which were similar to that of Pt (0.196 nm) and that of Rh (0.190 nm). PXRD (Figure S6 in SI) demonstrated that the Pt−Pd−Rh NCs were fcc-structured metals, and no crystallized impurities presented. The (111) peaks of Pt−Pd−Rh NCs fell between that of Rh and that of Pt. ICP-AES as well as XPS analysis with a penetration depth of ca. 2 nm were performed to determine the bulk composition and surface composition of Pt−Pd−Rh NCs, respectively (Table S2 in SI). ICP-AES results showed that the percentage of Rh component in NCs was significantly lower than that in precursors, indicating that not all

DOI: 10.1021/cs5018419
ACS Catal. 2015, 5, 1995−2008

the Rh(III) in the precursors were reduced during the syntheses. Compared with bulk composition, XPS results demonstrated a surface enrichment of the Rh component. Also, z-contrast from HAADF-STEM images (Figure 3a, Figures S4c

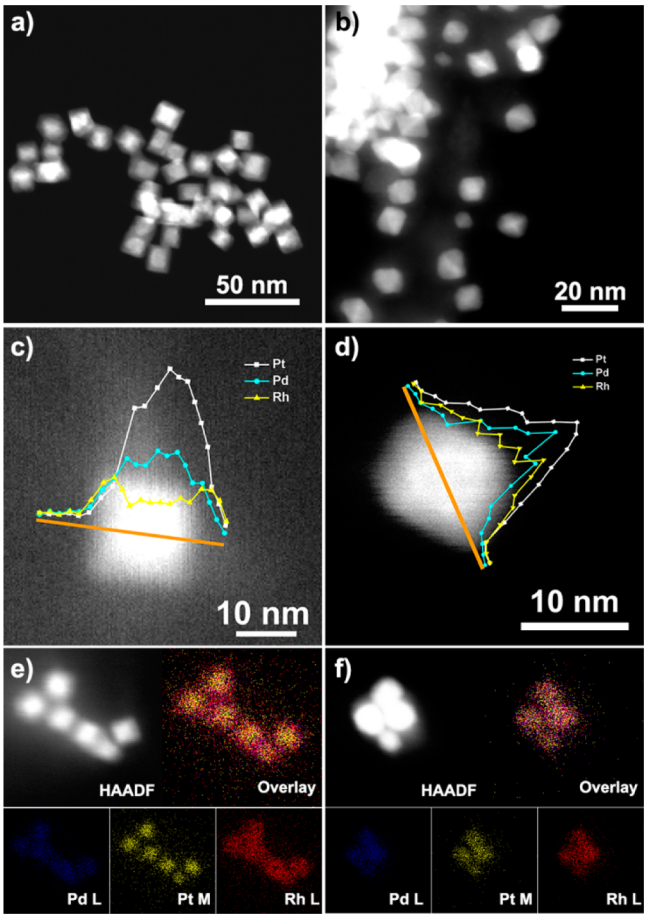

Figure 3. HAADF-STEM images of (a) PtPdRh NCs and (b) PtPdRh NTOs; EDS line scan profiles of (c) PtPdRh NCs and (d) PtPdRh NTOs; EDS element mapping images and their corresponding STEM images of (e) PtPdRh NCs and (f) PtPdRh NTOs.

in SI) illustrated that Pt was located mainly at the center of the NCs. According to EDS line scan profiles of a single trimetallic NCs and elemental mapping images (Figures 3c, 3e, Figures S 4d, S4e in SI), Pt and Pd mainly stayed at the center of the particles, whereas Rh segregated on the surface. It was consistent with XPS results. Hence, the trimetallic NCs possibly held a segregated PtPd@Rh structure.

A similar method was applied in the synthesis of 11.9 ± 1.1 nm PtPdRh NTOs with the addition of KBr (Figure 1b and Figure S2b in SI). The HRTEM image (Figure 1d) illustrated that the single-crystalline nanocrystals were bounded with eight (111) planes dominantly. PXRD confirmed that PtPdRh NTOs hold an fcc structure (Figure S6 in SI). HAADF-STEM EDS line scan profile and elemental mapping image (Figure 3d,f) clarified that NTOs hold a near homogeneous alloyed structure. The contrast of HAADF-STEM image (Figure 3b) also confirmed the near homogeneous element distribution. However, XPS result (28:14:58 for Pt/Pd/Rh, Table S2 in SI) demonstrated that there was an enhancement of Rh on the surface of PtPdRh NTOs compared with ICP-AES data (Pt/Pd/Rh ratio of 39:33:28). However, the surface segregation of Rh was much lower than that in NCs (Pt/Pd/Rh ratio of 7:10:83 for PtPdRh NCs). As illustrated in Figure S5, (111)-terminated Pt_3PdRh NTOs (6.0 ± 0.8 nm) and $PtPd_3Rh$ NTOs (7.5 ± 1.1 nm) were fabricated in high selectivity. XPS results (Table S2 in SI) showed that the surface composition of Pt_3PdRh NTOs (70:16:14 for Pt/Pd/Rh) was the same as its bulk composition (62:20:18 for Pt/Pd/Rh) determined by ICP-AES analysis, as well as for $PtPd_3Rh$ NTOs, suggesting that Pt−Pd−Rh NTOs were in a more uniform element distribution than Pt−Pd−Rh NCs (i.e., the surface composition was more close to the bulk composition).

Furthermore, owing to the segregated structure of Pt−Pd−Rh NCs prepared at 180 °C, Pt−Pd−Rh NCs with more homogeneous element distribution (PtPdRh NCs-200) were synthesized by elevating the reaction temperature in order to determine the influence of element distribution toward EOR and exclude the other factors from shape effect as illustrated in Figure S7.

3.4. Atomic-Level Element Distribution of Shaped Pt−Pd−Rh Nanocrystals. In order to clarify the local structure of each type of atoms, the first-shell coordination environment of Pt, Pd, and Rh in the ternary metal nanocrystals was analyzed by EXAFS (Figure S8, Table S3 in SI). Interatomic distance (R) and corresponding coordination number (CN) in the first coordination shell obtained from real space data fitting are summarized in Table 1. According to the first-shell fitting in

Table 1. EXAFS Parameters of Shaped Pt−Pd−Rh Nanocrystals

sample	edge	shell	CN	R (Å)
PtPdRh NCs	Pt L_3	Pt−Pt	7.5 ± 0.5	2.746 ± 0.003
		Pt−Pd	2.5 ± 0.3	2.739 ± 0.005
	Pd K	Pd−Pd	7.0 ± 0.5	2.733 ± 0.003
		Pd−Pt	2.5 ± 0.3	2.739 ± 0.005
	Rh K	Rh−Rh	8.3 ± 0.4	2.689 ± 0.002
PtPdRh NTOs	Pt L_3	Pt−Pt	4.6 ± 0.5	2.728 ± 0.007
		Pt−Pd	1.2 ± 0.7	2.74 ± 0.02
		Pt−Rh	3.3 ± 0.5	2.701 ± 0.008
	Pd K	Pd−Pd	8.0 ± 1.3	2.741 ± 0.009
		Pd−Pt	1.2 ± 0.7	2.74 ± 0.02
	Rh K	Rh−Rh	4.4 ± 0.3	2.694 ± 0.005
		Rh−Pt	3.3 ± 0.5	2.701 ± 0.008

PtPdRh NCs, Rh−Pt or Rh−Pd shells were undetected. Only Rh−Rh shells could be assigned from the fitting so Rh was segregated in the particles. In PtPdRh NCs, both CN_{Pt-Pt}/CN_{Pt-Pd} and CN_{Pd-Pd}/CN_{Pd-Pt} were close to 3:1, indicating that Pt and Pd were segregated into Pt-rich and Pd-rich domains at atomic level. In PtPdRh NTOs, although CN_{Pd-Pd}/CN_{Pd-Pt} was up to about 6.5:1, CN_{Pt-Pt}/CN_{Pt-M} (M = Pd, Rh) and CN_{Rh-Rh}/CN_{Rh-M} (M = Pt, Pd) decreased to about 1:1 and 1.3:1, respectively, as compared with PtPdRh NCs. Near half of both Pt and Rh alloyed to other type of atoms, verifying a more homogeneous atomic-level element distribution and stronger interactions among the three atoms at Rh-rich surface in PtPdRh NTOs than those in PtPdRh NCs. The coordination environment of each component in the Pt−Pd−Rh nanocrystals calculated from EXAFS analysis was consistent with the prior conclusions drawn from both XPS and EDS analyses.

Furthermore, to understand the origin of the difference on the element distribution of the samples with the two kinds of morphologies, shape and composition evolutions of these two

DOI: 10.1021/cs5018419
ACS Catal. 2015, 5, 1995−2008

kinds of nanostructures were monitored. Among the three elements, the Rh(III)/Rh pair has the lowest standard reduction potential ($E^{\theta}(RhCl_6^{3-}/Rh)$ = 0.5 V, $E^{\theta}(PdCl_4^{2-}/Pd)$ = 0.62 V, $E^{\theta}(PtCl_6^{2-}/Pt)$ = 0.742 V).[53] Therefore, Rh preferred to segregate on the surface of the particles, as it was the last element to be reduced. TEM and EDS were conducted to track the morphology and composition evolutions of Pt−Pd−Rh NCs under a series of reaction times (Figure S9 in SI). Within a 1.5 h reaction, the same amount of Pt and Pd precursors were reduced. $RhCl_3$ was mainly reduced during the next 2.5 h, which occurred with the formation of cubic morphology. It confirmed that the successive reduction of precursors was the reason for the segregated compositions.

However, NTOs exhibited more uniform surface element distribution than NCs at atomic level despite the same total composition and similar synthetic methods. According to the output from tracking the formation process of Pt−Pd−Rh NTOs (Figure S10 in SI), Pd (II) was preferentially reduced among the three precursors (Figure S10f in SI), and the obtained Pd-rich seeds (60% of Pd) were mostly octahedrons (Figure S10a in SI) with 30% of Pt and 10% of Rh, which agreed well with the first-shell coordination environment of Pd in PtPdRh NTOs. Compared to the yields (ratio of the amount of each element in nanoparticles to its total amount) in PtPdRh NCs at half an hour, the reduction of Rh(III) and Pt (IV) in PtPdRh NTOs was retarded with the absence of iodine. Followed by the reduction of Pt (IV) and Rh (III), multipod nanocrystals were generated from the octahedral seeds by the epitaxial growth on the corner sites. During the prolonged reaction time, the void between the pods with an abundance of defect sites was gradually filled by the reduction of residual metal ions or the diffusion of surface atoms,[33] as illustrated in Figure S10d. Hence, a more homogeneous element distribution was obtained due to the coreduction of Pt(IV) and Rh(III) and the promoted surface diffusion. In brief, the spatial element distributions of the two morphologies were attributed to their distinct growth mechanisms, as depicted in Figure S11.

3.5. Evolution of Surface Composition during Cyclic Voltammetry Measurements. PtPdRh NCs, Pt_3PdRh NCs, PtPdRh NCs-200, PtPdRh NTOs, Pt_3PdRh NTOs, and $PtPd_3Rh$ NTOs were selected as the model trimetallic catalysts for EOR to study the possible composition- and morphology-dependent catalytic properties with commercial Pt black (Alfa Aesar), Pd/C, Rh NCs, Pt−Pd NCs, and Pt−Rh NCs as references (Figure S12 in SI shows TEM images of references). Figures S13b and S13c show the stable cyclic voltammograms of all samples in 0.1 mol·L^{-1} $HClO_4$ aqueous solution, which were utilized to determine the ECSA.

The peaks between 0.34 and 0.72 V at the negative-going potential scan referred to the reduction of adsorbed oxygen species, which suggested the surface composition of the catalysts.[54] When the catalysts reached electrochemical steady states after a hundred cycles of CV measurements, all the reduction peaks shifted to the high potential, implying a decrease of Rh component on the Rh-rich surfaces (Figure S13a, S13b, and Table S4 in SI). It has been suggested that the reduction peak shifted more positively with less Rh on surface according to previous reports.[54] EDS results (Table S5 in SI) of the Pt−Pd−Rh NPs after catalysis demonstrated a slight decrease of Rh on bulk, and the EDS line scan profile of PtPdRh NCs after reaction (Figure S14 in SI) showed a slight enrichment of Pt on the surface. TEM images (Figure S15 in SI) show facets of the shaped nanoparticles mostly maintained during the catalysis with the removal of the corner site atoms, which were highly coordination-unsaturated and considered as unstable sites under electrochemical tests.[55] Therefore, unlike the reconstruction reported in Au−Pd NPs,[56] surface leaching of Rh would be the major reason for the change of surface composition during the catalysis rather than a migration of Rh from surface to the core.

Because the oxide reduction peak potential of Pd (0.62 V) was close to that of Pt (0.72 V) (Figure S13c in SI), the potential values of oxide reduction peaks reflected the surface composition of trimetallic nanocrystals, especially for Rh content. The steady potential values of oxide reduction peaks for composition-varied Pt−Pd−Rh NPs in the cathodic scan in 0.1 M $HClO_4$ solution followed the order: Pt_3PdRh NTOs ≈ Pt_3PdRh NCs > PtPdRh NTOs ≈ $PtPd_3Rh$ NTOs ≈ PtPdRh NCs-200 > PtPdRh NCs, indicating that the surface compositions of the alloyed surface after reactions were still correlated with the initial surface compositions obtained from XPS despite of the leaching of Rh. As illustrated in Figure S13b, there was only one apparent reduction peak in the cathodic scan for the trimetallic NPs. It suggested that the three elements were alloyed rather than segregated on the surface of Pt−Pd−Rh nanocatalysts during the reactions. Hence, we ruled out the influence of element distribution status (mixing homogeneity) on the surface in the mechanism study and assumed that the three elements were well alloyed on the surface layer. The element distribution mentioned below referred to the element distribution in radial direction of a particle.

3.6. Activities of Shaped Pt−Pd−Rh NPs toward EOR. As illustrated in Figure 4a, linear sweep voltammograms (LSVs) from 0 to 0.8 V at a sweep rate of 1 mV·s^{-1} in 0.1 M $HClO_4$/0.5 M CH_3CH_2OH solution were applied to obtain the quasi-steady-status polarization curves. ECSA of all the tested samples were listed in Table S6, and ECSA normalized current density values at 0.5 V versus NHE were used to judge the overall activity (Table 2, and Table S6 in SI) as referred to the related literatures in regard to EOR catalysts.[24,28] Additional current density values at other potentials were summarized in Table S6.

PtPdRh NTOs, Pt_3PdRh NTOs, and 8.8 nm PtPdRh NCs-200 were the three most active Pt−Pd−Rh nanocatalysts at 0.5 V vs NHE, and the activity was increased to about 5 times as compared with that of commercial Pt black (0.0093 mA·cm^{-2}). In addition, at a higher potential, 8.8 nm PtPdRh NCs-200 exhibited better activity than PtPdRh NTOs and Pt_3PdRh NTOs. Furthermore, 13.8 nm PtPdRh NCs-200 and Pt_3PdRh NCs showed as much as 3 times and twice activities than commercial Pt black, respectively, which were regarded as the second best Pt−Pd−Rh nanocatalysts that we obtained. $PtPd_3Rh$ NTOs, PtPd NCs, 18.5 nm PtPdRh NCs-200, and PtRh NCs showed comparable activity with commercial Pt black. However, PtPdRh NCs, which were synthesized at 180 °C, had little EOR activity at 0.5 V.

With the consideration of morphology, (111)-terminated Pt−Pd−Rh NTOs were more active than (100)-terminated Pt−Pd−Rh NCs-200 with similar sizes. For cubic shape, it seemed that the more homogeneous element distribution achieved by elevated temperature can be attributed to the promoted activity of PtPdRh NCs-200. Additionally, a size effect was observed in PtPdRh NCs-200. Enrichment of surface Pt content in Pt−Pd−Rh NTOs and Pt−Pd−Rh NCs would also give rise to the enhanced EOR activity, especially for

DOI: 10.1021/cs5018419
ACS Catal. 2015, 5, 1995−2008

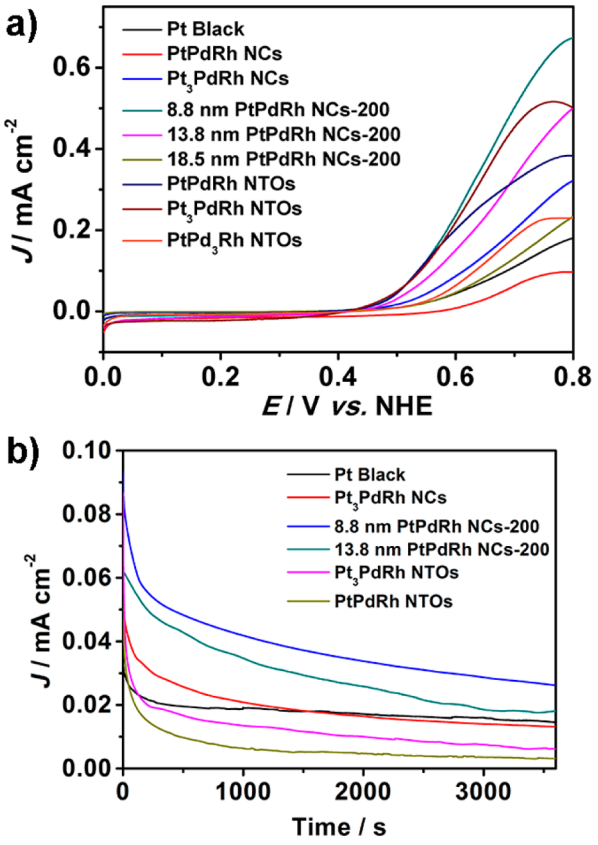

Figure 4. (a) LSVs curves of shaped Pt−Pd−Rh NPs in 0.5 M CH_3CH_2OH/0.1 M $HClO_4$ solution at a sweep rate of 1 mV·s^{-1}. (b) Chronoamperometric curves of selected Pt−Pd−Rh NPs at 0.5 V vs NHE in 0.5 M CH_3CH_2OH/0.1 M $HClO_4$ solution.

PtPdRh NCs. Therefore, geometric structure, particle size, element distribution, and composition were deduced to be the key factors to influence the EOR activity of Pt−Pd−Rh nanocatalysts and would be discussed in detail in the following sections.

The mass activities of active Pt−Pd−Rh nanocatalysts at 0.5 V versus NHE normalized by the mass of Pt and noble metals were, respectively, given in Table S7. Mass activities normalized by overall metals should be applied into the comparison, because the elemental abundance of Rh and Pd was as low as that of Pt. It was reasonable that all the solid Pt−Pd−Rh NPs with well-shaped morphologies possessed smaller surface areas (i.e., ECSA/mg_{metal}) than commercial Pt black with high surface area despite of their contained lighter metals (i.e., Pt and Rh). As a result, Pt_3PdRh NTOs (2.38 mA·mg_{metal}^{-1}), PtPdRh NTOs (1.85 mA·mg_{metal}^{-1}), and Pt_3PdRh NCs (1.83 mA·mg_{metal}^{-1}) only showed a slight higher mass activity at 0.5 V than commercial Pt black (1.64 mA·mg_{metal}^{-1}), although these trimetallic NPs had much higher specific activity.

In addition, chronoamperometric experiments recorded at 0.5 V vs NHE were carried out on Pt−Pd−Rh nanocatalysts with enhanced activity to evaluate the durability. As illustrated in Figure 4b and Table 2, all the five Pt−Pd−Rh nanocatalysts possessed enhanced current densities at the initial time as compared with commercial Pt black, whereas there was a negligible change on activity order. The current densities of (111)-facet-terminated PtPdRh NTOs and Pt_3PdRh NTOs at 1 h reduced to 6% and 7% of the initial ones, respectively, and were inferior to that of Pt black. However, the current density of 8.8 nm PtPdRh NCs-200 at 1 h was almost twice as much as that of Pt black, and those of 13.3 nm PtPdRh NCs-200 and Pt_3PdRh NCs were close to that of Pt black. Hence, an apparent shape effect on durability was disclosed: (100)-enclosed Pt−Pd−Rh NCs, which were synthesized at 200 °C, maintained more than 25% activity at 1 h, suggesting a superior durability of Pt−Pd−Rh (100) facets over (111) facets. The capability to oxidize CO_{ad} on different Pt crystal planes and accumulation of Rh−C containments on Rh (111) surface well-interpreted the shape effect on EOR durability of shaped Pt−Pd−Rh nanocatalysts.[37,57,58] The 5 h chronoamperometric experiments at 0.7 V were also conducted on these EOR catalysts, as shown in Figure S16 and Table S8. All the trimetallic catalysts exhibited lower current densities than commercial Pt black, and 8.8 nm PtPdRh NCs-200 still possessed the best durability among all the Pt−Pd−Rh NPs. (100)-Terminated NCs and Pt-rich NPs showed good durability as compared with the other Pt−Pd−Rh NPs, so similar shape effect and composition effect on durability were also observed at high potential. As determined from the shape of chronoamperometric curves, Pt black deactivated quickly initially and reached equilibrium rapidly, and it took almost 2 h for Pt−Pd−Rh NPs to level off. It indicated a slow accumulation process of obstacle species on Pt−Pd−Rh NPs.

3.7. Synergistic Effect of Faceted Pt−Pd−Rh NPs toward EOR. As indicated by DFT calculations and activity evaluations of the well-shaped Pt−Pd−Rh NPs, a synergistic effect among Pt, Pd, and Rh toward EOR was proposed. To identify the influence of each component, EOR properties of Rh NCs, Pt−Rh NCs, Pt−Pd NCs, and Pd/C were measured by the same LSVs method (Figure S17a and Table S6 in SI). Compared with Pt black, Pd/C catalysts exhibited negligible current density (1.2×10^{-4} mA·cm^{-2}) at 0.5 V, manifesting

Table 2. Current Density Values of Commercial Pt Black and Selected Pt−Pd−Rh Nanocrystals at 0.5 V Obtained from LSVs and 1 h Chronoamperometric Tests

catalysts	J at 0.5 V vs NHE (LSVs) (mA·cm^{-2})	$J_{Initial}$ at 0.5 V vs NHE (mA·cm^{-2})	J_{1h} at 0.5 V vs NHE (mA·cm^{-2})
Pt Black	0.0093	0.0351	0.0146
PtPdRh NCs	~0	/	/
Pt_3PdRh NCs	0.0169	0.0515	0.0132
8.8 nm PtPdRh NCs-200	0.0460	0.0933	0.0263
13.8 nm PtPdRh NCs-200	0.0308	0.0622	0.0176
18.5 nm PtPdRh NCs-200	0.0088	/	/
PtPdRh NTOs	0.0447	0.0527	0.0031
Pt_3PdRh NTOs	0.0491	0.0867	0.0061
$PtPd_3Rh$ NTOs	0.0090	/	/

DOI: 10.1021/cs5018419
ACS Catal. 2015, 5, 1995−2008

that pure Pd nanocatalyst was inert toward EOR in acidic solution. Unexpectedly, monometallic Rh NCs possessed similar activity (0.012 mA·cm^{-2}) at 0.5 V as Pt black, indicating that both the Rh site and Pt site contributed equally to the EOR activity at low potential in acidic solution. It was deduced that EOR activity of Rh NCs near onset potential probably resulted from its outstanding capability on the cleavage of C−C bond of ethanol. However, the current density of Rh NCs started to drop at 0.6 V, whereas that of Pt black still increased with the increase of potential. As a consequence, the activity of Rh sites was usually overlooked near the first oxidation peak of Pt catalysts in the previous reports.[59] On account of the elaborate discussions on the roles of Pt and Rh in the published research, as well as our coincident results,[14−16] the following discussion will be focused on the role of Pd.

Besides the monometallic nanocatalysts, (100)-terminated bimetallic Pt−Rh NCs and Pt−Pd NCs were selected to further rationalize the possible synergistic effect between two of the elements. As illustrated in Figure S17a and Table S6, the LSVs curves almost overlapped below 0.6 V, as Pt−Rh NCs showed higher reactivity than Pt−Pd NCs at high potential. It demonstrated that incorporation of Pd promoted the reactivity of Pt sites probably due to the modulation of electronic structure[29] because inactive Pd sites on the surface were taken into the calculation of ECSA for Pt−Pd NCs. For Pt−Rh NCs, there was no obvious promotion on activity when alloying Pt with Rh, when considering the similar specific activity of Pt black and Rh NCs catalysts.

Based on chronoamperometric experiment results of reference nanocatalysts at 0.5 V (Figure S17b and Table S8 in SI), Rh NCs and Pt−Rh NCs only retained less than 15% of the initial activity at 1 h, whereas the current density of Pt−Pd NCs reduced to 41% of the initial one. It was concluded that Rh components made the EOR catalysts much unstable under the action of long-time constant potential due to the accumulation of the Rh−C obstacle.[41,57] Nevertheless, compared with the performance of PtRh NCs and PtPdRh NCs-200, both the activity and durability of Pt−Rh-based catalysts were improved with the introduction of Pd, which was inert to EOR. Hence, a synergistic effect among Pt, Pd, and Rh toward EOR was certified by the catalytic performance evaluations of monometallic and bimetallic nanocatalysts. In view of the synergistic effect between Pt and Pd toward MOR and EOR, the enhanced reactivity was probably related to the modulated electronic structure that weakened adsorption of carbonic species (e.g., CH_x, CO, etc.) and supply of hydroxyl group to facilitate the oxidation of adsorbed carbonic species at low potential.[26,29,60]

In short, Pt and Rh were proved to be the primary active sites to EOR in acidic solution, whereas PtRh catalysts suffered from the accumulation of adsorbed carbonic species and the resulting inferior durability. Inactive Pd was proposed to be an auxiliary site that offered hydroxyl groups at low potential and modulated the electronic structure to facilitate the oxidation of adsorbents, so the EOR performance of catalysts was significantly promoted by the construction of trimetallic Pt−Pd−Rh nanocatalysts.

3.8. Influence of Morphology, Element Distribution, Particle Size, and Composition. Geometric structure and element distribution (i.e., the difference between the inner composition and outer composition in a particle), as mentioned above, were demonstrated to be the key factors to influence the EOR activity of Pt−Pd−Rh nanocatalysts. Ahead of the discussion on shape effect, the influence of element distribution ought to be figured out because Pt−Pd−Rh NCs and NTOs prepared at 180 °C had quite different element distribution status. The catalytic performance evaluation on PtPdRh NCs-200 with more uniform element distribution and similar average size (13.8 nm PtPdRh NCs-200) was carried out to interpret the influence of element distribution. XPS analysis was applied in the determination of element distribution in particles, as the mismatch between surface composition and bulk composition reflected the element arrangement in a particle on the premise that metals were randomly alloyed on surface layers. Element distribution status judged from XPS was in accordance with atomic-level element distribution obtained from EXAFS analyses and single-particle EDS analyses. 13.8 nm PtPdRh NCs-200 were prepared by the similar hydrothermal method with the increase of temperature to 200 °C. According to previous reports, high temperature could draw the redox capabilities of metal precursors near and brought about homogeneous element distribution in the particles.[61] XPS results manifested an improved element distribution of 13.8 nm PtPdRh NCs-200 with a Pt/Pd/Rh atomic ratio of 15:25:60 on the surface, less segregated than PtPdRh NCs prepared at 180 °C with a Pt/Pd/Rh atomic ratio of 7:10:83 on the surface(Table S2 in SI). The EOR specific activity of 13.8 nm PtPdRh NCs-200 at 0.5 V was 0.031 mA·cm^{-2}, but PtPdRh NCs synthesized at 180 °C showed no activity. It was verified that more interatomic interfaces created by the improvement in element distribution gave rise to the high reactivity as DFT simulation predicted.

Influence of particle size and composition to EOR could be ignored in the comparison of 11.9 nm PtPdRh NTOs and 13.8 nm PtPdRh NCs-200, because the surface compositions before and during electro-catalysis was close to those of PtPdRh NTOs in light of XPS results and stable CV curves in $HClO_4$. However, the activity of 13.8 nm PtPdRh NCs-200 (0.031 mA·cm^{-2}) was still lower than that of PtPdRh NTOs (0.0447 mA·cm^{-2}), suggesting that exposed facets as well as element distribution probably contributed to the improved activity of PtPdRh NTOs. Compared with Pt_3PdRh NCs which had the same initial surface composition (Pt/Pd/Rh molar ratio of 34:11:55) as PtPdRh NTOs (Pt/Pd/Rh molar ratio of 28:14:58), the higher activity of PtPdRh NTOs also confirmed the merits of (111) exposed facet. As illustrated in Figure 4a, the oxidation peak potentials of Pt−Pd−Rh NTOs fell in the region between 0.7 and 0.8 V, whereas those of Pt−Pd−Rh NCs were higher than 0.8 V. At 0.8 V, 13.8 nm PtPdRh NCs-200 and 8.8 nm PtPdRh NCs-200 showed higher activity than Pt−Pd−Rh NTOs. This implied that Pt−Pd−Rh NTOs exhibited high EOR activity at low potential (below 0.7 V, i.e., the oxidation peak potential), and Pt−Pd−Rh NCs showed strong capability to EOR at high potential. Furthermore, the (100) facet of Pt−Pd−Rh NCs remarkably increased the durability at constant potential. Therefore, the exposed facet of shaped Pt−Pd−Rh NPs affected the activity at varied potentials as well as the durability, suggesting the alteration of accumulated adsorbents on the two facets. The intrinsic mechanism will be discussed subsequently in the in situ FTIR study.

In addition, 8.8, 13.8, and 18.5 nm PtPdRh NCs-200 with the same overall composition were synthesized by the adjustment of halide ions. Due to the relative large particle size (i.e., 9−18 nm) and well-defined morphology of PtPdRh NCs-200, the influence of special reaction sites (e.g., terrace sites,[62] etc.)

DOI: 10.1021/cs5018419
ACS Catal. 2015, 5, 1995−2008

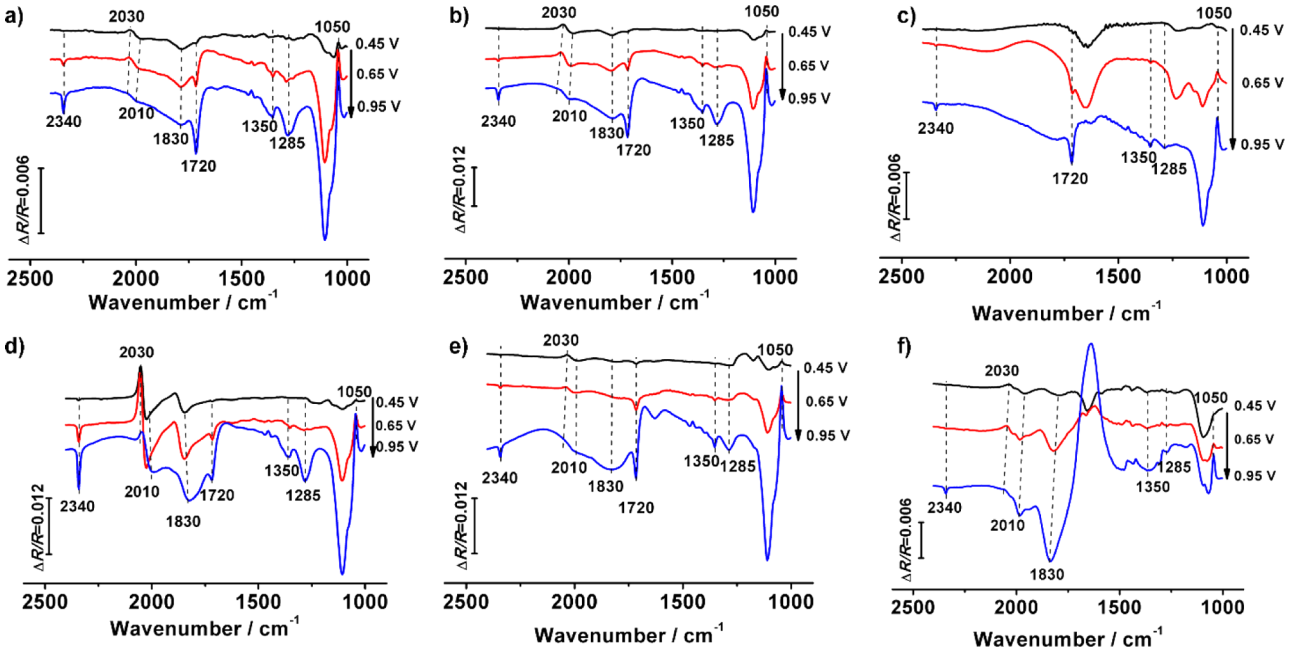

Figure 5. In situ FTIR spectra of (a) PtPdRh NCs, (b) Pt_3PdRh NCs, (c) PtPdRh NCs-200, (d) PtPdRh NTOs, (e) Pt_3PdRh NTOs, and (f) $PtPd_3Rh$ NTOs at different potentials in a mixture of 0.5 M ethanol and 0.1 M $HClO_4$.

brought by small size could be ignored. The EOR activity at 0.5 V increased with the decrease of particle sizes. XPS analysis clarified that the Pt/Pd/Rh ratio on the surface approached 1:1:1 with reduced particle size, indicating the homogeneous element distribution status of 8.8 nm PtPdRh NCs-200. It accorded with the studies on size effect to element distribution of nanoparticles.[63,64] DFT simulations also suggested an increased activity from Rh-rich to the region with Pt/Pd/Rh molar ratio of 1:1:1, consistent with the change on surface compositions of PtPdRh NCs-200. Hence, the improved element distribution status brought by small size was the probable key reason for the size effect of PtPdRh NCs-200. In other words, the catalytic performance of PtPdRh NCs-200 with varied sizes confirmed the influence of element distribution to EOR in Pt−Pd−Rh nanocrystals.

To correlate the activities of composition-varied Pt−Pd−Rh NPs with previous DFT simulations, evaluation results acquired at low potential (0.5 V) were used due to the probable uncertainty brought by the applied potentials.[51] Among all the shaped Pt−Pd−Rh trimetallic nanocatalysts, enhanced activity at 0.5 V was observed on NPs with a Pt/Pd/Rh molar ratio of 1:1:1 and 3:1:1 on overall composition. However, the activity of Pd-rich $PtPd_3Rh$ NTOs equaled to that of Pt black. Even worse, Pt−Pd−Rh NPs with a Rh-rich surface (i.e., PtPdRh NCs) were inactive below 0.5 V but active at higher potential. In view of DFT calculations, it was noted that the Pt−Pd−Rh (100) surface with Pt/Pd/Rh molar ratio of 1:1:1, Pt−Pd−Rh (100) surface with Pt/Pd/Rh molar ratio of 1:1:1 or 7:1:1, and Pd-rich Pt−Pd−Rh (100) and (111) surface were probably favored for EOR. Judging from XPS results, the Pt/Pd/Rh molar ratio of Pt_3PdRh NCs on the surface was closer to 1:1:1 than that of PtPdRh NCs, agreeing with the DFT simulation results that the capability on cleavage of C−C bond increased from Rh-rich region to the Pt/Pd/Rh molar ratio of 1:1:1. Therefore, Pt_3PdRh NCs were the better cubic Pt−Pd−Rh catalysts prepared at 180 °C. The size effect of PtPdRh NCs-200 was another compelling evidence for the optimal surface composition. For (111)-terminated Pt−Pd−Rh NTOs, the surface composition was correlated to the corresponding bulk composition due to the relative homogeneous element distribution. It was a matter of course that enhanced overall activity was obtained for Pt−Pd−Rh NTOs with Pt/Pd/Rh molar ratio of 28:14:58 and 70:16:14 on the surface by XPS, which approached the appropriate composition of (111) planes for breakdown of C−C bond and oxidation of CO_{ad}, respectively, referring to the DFT simulation results on Pt−Pd−Rh (111) planes. For the Pd-rich region, the experimental results appeared not to be consistent with theoretical simulations. Nearly 60% of the surface atoms of $PtPd_3Rh$ NTOs were covered with EOR-inert Pd sites, so activity enhancement did take place for only Pt or Rh sites. Meanwhile, other essential steps for EOR (i.e., dehydrogenation, CO_{ad} oxidation, which Pd site might show inferior capability to catalyze) may retard the overall reactivity on Pd-rich NPs.

For all the selected (100)-terminated Pt−Pd−Rh NCs, it was noted that the polarization curves were in a similar shape and the activities changed with their surface compositions acquired from XPS analyses, basically corresponding to the DFT simulations on composition-varied Pt−Pd−Rh (100) planes. Hence, promotion on activity through elevating element distribution for Pt−Pd−Rh NCs possibly stemmed from the optimal surface composition with reduced Rh content. To sum up, it was revealed that element distribution, particle size, exposed facets, and composition significantly affected the EOR performance of Pt−Pd−Rh NPs. Among these factors, except for shape effect, particle size, element distribution, and overall composition were tightly associated with surface composition given by XPS with the assumption that surface atoms were randomly alloyed under reaction conditions. Therefore, geometric structure and surface composition should be considered as the two vital parameters for the EOR performance of shaped Pt−Pd−Rh NPs.

3.9. In Situ FTIR Study To Determine the Selectivity to CO_2.

To further understand the structure- and composition-

DOI: 10.1021/cs5018419
ACS Catal. 2015, 5, 1995−2008

dependent catalytic properties of trimetallic Pt−Pd−Rh nanocrystals, in situ FTIR was performed to detect the intermediates and to rationalize the mechanism. PtPdRh NCs, Pt_3PdRh NCs, 13.8 nm PtPdRh NCs-200, Pt_3PdRh NTOs, PtPdRh NTOs, $PtPd_3Rh$ NTOs, and Pt black were selected to verify the possible intrinsic mechanism. Figure S18 shows the in situ FTIR spectra under a continuous stepped potential from 0.25 to 0.75 V. Considering the probable accumulation of catalytic dead-end products during in situ IR tests in static conditions,[65,66] we cleaned the surface of the working electrode by deionized water after the measurement at each potential in order to reduce the interference of such dead-end products from the previous potential and qualitatively estimate the selectivity. The obtained spectra and magnified ones are illustrated in Figure 5, Figure S19 and Figure S20 respectively. All the assignments of the characteristic bands are listed in Table S9 according to previous reports.[18,67]

In Figure S18, in situ FTIR spectra under a continuous stepped potential distinctly illustrated the adsorbed intermediates during reactions and the corresponding onset potentials. The onset potentials of CO_2 on Pt−Pd−Rh NTOs were near 0.35, 0.1, and 0.2 V, which were negatively shifted as compared with Pt black and Pt−Pd−Rh NCs, respectively. It implied that (111)-terminated Pt−Pd−Rh NTOs possessed the capability to fully oxidize ethanol at extremely low potential. It was noted that the band of CO_{ad} at 2030 cm^{-1} (linear CO_{ad}) and 1830 cm^{-1} (bridge CO_{ad}) appeared at 0.25 V in the spectra of Pt−Pd−Rh NTOs ensured the capability on the cleavage of C−C bond at low potential for Pt−Pd−Rh NTOs. In addition, strong linearly bounded CO_{ad} was observed on Pt_3PdRh NCs above 0.25 V (Figure 5b, and Figure S18c in SI), whereas the formation of CO_2 started from 0.55 V, probably due to the insufficient ability on CO_{ad} oxidation at low potential. The onset potentials of acetic acid and acetaldehyde (ca. 0.65 V) were quite similar for all the samples, judging from the bands positioned at 1285, 1350, and 1720 cm^{-1}. All these band intensities increased with the elevated applied potential, so scarcely any conversions between the adsorbents could be decided from the band intensities. The spectra obtained at individual potential (Figure 5 and Figure S19 in SI) were identical with the spectra under the continuous stepped potential (Figure S18).

A blue shift on the band of CO_{ad}, which is known as the "Stark effect", was observed with the increased applied potential in Figure 5, S18, and S20, .[68] As shown in Figure S21, Stark tuning rates, the relationship between applied potential and vibration frequency, were associated with the surface coverage of CO_{ad}. However, unlike pure CO adsorbed on the surface of monometallic plane, the situation was more complicated for nanosized particles in the dissociation of organic compounds, and Stark tuning rates were only applied to compare the CO_{ad} coverage qualitatively. In general, the Stark tuning rates at low potential were higher than those at high potential for each catalyst. In terms of previous reports, high Stark tuning rate suggested a low CO coverage (i.e., less than 0.13 monolayer for 45 $cm^{-1}\cdot V^{-1}$ on a polycrystalline Pt electrode in 0.1 M $HClO_4$), and the low value suggested a high CO_{ad} coverage.[27,68] The turning points of these plots fell between 0.55 and 0.75 V, implying that a high coverage of CO_{ad} on Pt−Pd−Rh catalysts in the region from 0.55 to 0.95 V. The values of the upward linearly bonded CO_{ad} band at low potential followed the order: Pt_3PdRh NCs (66 cm^{-1} V^{-1}) ≈ Pt_3PdRh NTOs (66 cm^{-1} V^{-1}) > $PtPd_3Rh$ NTOs (39 cm^{-1} V^{-1}) ≈ PtPdRh NTOs (39 cm^{-1} V^{-1}), indicating the same sequence of CO_{ad} kinetics on the catalysts and a possible composition effect.[27] Hence, adsorbed CO on the surface was an appreciable obstacle for these catalysts toward EOR, especially for $PtPd_3Rh$ NTOs and PtPdRh NTOs. This probably depressed the activity and durability of Pt−Pd−Rh NTOs, particularly at high potential with high CO_{ad} coverage. The CO_2 and CO_{ad} band appearing at 0.25 V on Pt−Pd−Rh NTOs demonstrated the capability of Pt−Pd−Rh (111) facets on the fully oxidation of ethanol as well as the cleavage of C−C bond. Furthermore, the deduced CO_{ad} oxidation capabilities were in agreement with the DFT simulations on Pt−Pd−Rh (111) facets for Pt−Pd−Rh NTOs (Figure 2f).

To determine the selectivity to total oxidized product CO_2 at 0.65 and 0.95 V, only the ratios of the band intensity of CO_2 at 2340 cm^{-1} to that positioned at 1285 cm^{-1} (acetic acid) were utilized as shown in Figure 6, Figure S22 and Table S10,

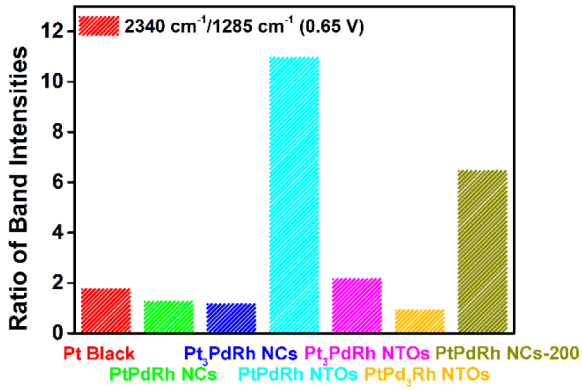

Figure 6. Ratios of in situ FTIR adsorption band intensities of CO_2 at 2340 cm^{-1} to that of acetic acid at 1285 cm^{-1} at 0.65 V.

because the band of C═O stretching vibration at 1715 cm^{-1}, which assigned to the formation of acetic acid and acetaldehyde, was perturbed by the bending mode of H_2O at 1650 cm^{-1}.[59] At 0.95 V, the band ratio of PtPdRh NTOs was slightly higher than the others, so there was no significant difference for the selectivity (Figure S22). It probably attributed to the domination of partial oxidation path with the formation of acetic acid at very high potential. Nevertheless, (111)-bounded PtPdRh NTOs exhibited the highest selectivity to CO_2 at 0.65 V, 6 times as much as that of commercial Pt black. It agreed well with previous DFT calculation on the superior capability of Pt−Pd−Rh (111) planes with Pt/Pd/Rh molar ratio of 1:1:1 in the cleavage of C−C (Figure 2b,d). However, despite the high selectivity of PtPdRh NTOs toward EOR, the activity of Pt_3PdRh which had inferior ability on the breakdown of C−C bond was slightly higher than that of PtPdRh NTOs, indicating that there ought to be another obstacle on EOR catalyzed by Pt−Pd−Rh NTOs. Choi et al. simulated the decomposition of ethanol on Rh (111) planes by DFT and kinetics Monte Carlo simulations.[41] They stated that the major obstacle of ethanol decomposition on Rh (111) was the C−C contamination instead of the breakdown of C−C bond. It gave a plausible explanation to the formation of CO_2 and CO species at low potential on PtPdRh NTOs. It demonstrated that the capability in the oxidation of CO_{ad} increased with the increasing Pt sites introduced in ternary NTOs by DFT simulations and the Stark tuning rates (Figure 2f, Figure S21 in SI), achieving the promoted EOR activity for Pt_3PdRh NTOs, along with the

DOI: 10.1021/cs5018419
ACS Catal. 2015, 5, 1995−2008

decrease on the capability in cleavage of C−C bond as testified by in situ FTIR (Figure 6). The result manifested the proposal on the possible obstacle of EOR Pt−Pd−Rh NTOs and provided another optimum EOR catalysts in the Pt−Pd−Rh system. A strong CO_{ad} band was observed in $PtPd_3Rh$ NTOs at 0.25 V, implying its superior capability on the breakdown of C−C bonds. However, its low selectivity to CO_2 possibly resulted from the confinement of other steps, such as the low CO_{ad} oxidation kinetics, which was indicated by Stark tuning rate and DFT simulation (Figure S21 in SI and Figure 2f). It gave a plausible explanation to the inferior activity of $PtPd_3Rh$ NTOs.

In addition, compared with PtPdRh NCs and 13.8 nm PtPdRh NCs-200 (Figure 6), the selectivity to CO_2 at 0.65 V increased 5-fold by homogenizing element distribution. DFT simulation of C−C bond splitting on (100) planes also suggested the lower reaction barrier at Pt/Pd/Rh ratio of 1:1:1 to Rh-rich region (Figure 2a,c). However, the selectivity of PtPdRh NCs-200 was almost half of that of PtPdRh NTOs, and the initial potential of CO_2 generation was higher than that of PtPdRh NTOs. It verified that both the exposed facet and the appropriate surface composition contributed to the strong capability of PtPdRh NTOs in the cleavage of C−C bond at low potential.

For the two best catalysts in selectivity, high CO_{ad} coverage and sluggish CO oxidation kinetics resulted in the poor durability of PtPdRh NTOs, as compared with 13.8 nm PtPdRh NCs-200. Unlike the other Pt−Pd−Rh NPs, it was noted that there was no sharp CO_{ad} band at diverse applied potential in Figure 5c, S18d, and S20g, indicating fast CO_{ad} oxidation kinetics on 13.8 nm PtPdRh NCs-200. Hence, the high CO_2 selectivity at 0.65 V should be partially attributed to the superior CO_{ad} oxidation capability. The 8.8 nm PtPdRh NCs-200 with more homogeneous element distribution ought to possess stronger capabilities in the breakdown of the C−C bond than the 13.8 nm PtPdRh NCs-200 in light of the optimal surface composition suggested by DFT simulations, and it further contributed to the high performance of 8.8 nm PtPdRh NCs-200.

On the basis of the associated analyses of FTIR, EOR evolution, and DFT simulation, a possible EOR mechanism on shaped Pt−Pd−Rh nanocrystals was put forward. At high potential (above 0.7 V), the coverage of CO_{ad} increased (Figure S21 in SI), and partial oxidation products (acetic acid) started to increase (Figure 5, Figure S18 and S19 in SI). In consideration of the literature[51] and selectivity given by FTIR (Figure S22 in SI), formation of oxidant (i.e., hydroxyl or oxygen atom) probably gave rise to the preferential partial oxidation path directly as the following equation:

$$Pt(CH_3CH_2OH)_{ad} + Pt(H_2O)_{ad} \rightarrow Pt + CH_3COOH + 4H^+ + 4e^- \quad (9)$$

High applied potential condition also facilitated the oxidization of the surface Rh and Pd sites rather than Pt sites, as judging from their reducing capacity. Hence, more surface sites would be hindered by CO_{ad}, O_{ad}, and OH_{ad} at high potential for Pt−Pd−Rh nanocrystals than pure Pt, when comparing the durability at 0.5 and 0.7 V. This resulted in the limited activity and poor durability for Pt−Pd−Rh nanocrystals at 0.7 V. Meanwhile, it was reasonable that Pt-rich NPs possessed high performance in activity and durability at high applied potential, as illustrated in Figure S16. Under low applied potential, adsorbed ethanol was proved to dissociate on a trimetallic surface to generate CO_{ad} species. Pt was usually considered as the site to capture unbounded ethanol and the place where dehydrogenation took place; the Rh site promoted the dissociation of C−C bond and was easily hindered by the formed CH_x group; the Pd site was revealed to facilitate the formation of hydroxyl group at low potential and assisted the cleavage of the C−C bond with Pt and Rh sites, as suggested by DFT simulations. Hence, the full oxidation reaction path of ethanol under low applied potential on Pt−Pd−Rh nanocrystals was deduced as

$$Pt + CH_3CH_2OH \rightarrow Pt(CH_3CH_2OH)_{ad} \quad (10)$$

$$Pt(CH_3CH_2OH)_{ad} \rightarrow Pt(CH_2CH_2O)_{ad} \text{ or } Pt(HCCO)_{ad} + H^+ + e^- \quad (11)$$

$$Pt(CH_2CH_2O)_{ad} \text{ or } Pt(HCCO)_{ad} + Rh + Pd \rightarrow Pt(CO)_{ad} + Rh(CH_x)_{ad} + Pd \quad (12)$$

$$Pd + H_2O \rightarrow Pd(OH)_{ad} + H^+ + e^- \quad (13)$$

$$Pt(CO)_{ad} + Pd(OH)_{ad} \rightarrow Pt + Pd + CO_2 + H^+ + e^- \quad (14)$$

$$Rh(CH_x)_{ad} + 2Pd(OH)_{ad} \rightarrow Rh + Pd + CO_2 + (2 + x)H^+ + (2 + x)e^- \quad (15)$$

Hence, the association of the three elements was essential for the fully oxidation of ethanol at low potential.

With the help of in situ FTIR and DFT calculation, the influence of the exposed facet and surface composition to the capability in the cleavage of C−C bond were revealed, and the possible reaction mechanism on shaped Pt−Pd−Rh nanocrystals was rationalized. DFT simulations were associated with experimental results at low applied potential, in spite of ignoring the influence of applied potential, solvent environment, and so on. Lastly, the increased activity of shaped Pt−Pd−Rh nanocrystals was correlated to the two possible obstacles: the cleavage of C−C bond was proposed to be the descriptor for the activity of (100)-bounded NPs; so were both the cleavage of C−C bond and the oxidation of CO for that of (111)-bounded NPs.

3.10. Comparison with Pt−Rh−Sn NPs. To the best of our knowledge, Pt−Rh−Sn ternary nanocatalysts have exhibited prominent EOR activity and have drawn increasing attention in the current research of EOR catalysts. Herein, we fabricated two kinds of Pt−Rh−Sn tricomponent nanocatalysts with the optimal Pt/Rh/Sn ratio of 3:1:4.[24,69] As illustrated in Figure S23, Pt−Rh−Sn NPs synthesized by the similar hydrothermal method (PtRh(Sn)/SnO_2 NPs) were revealed to be a mixture of fcc-structured Pt-based alloy and SnO_2 NPs. XRD (Figure S24 in SI) confirmed the constituents of as-obtained Pt−Rh−Sn NPs. The carbon supported Pt−Rh−Sn NPs synthesized by reported method (PtRhSn/C NPs) were also characterized by XRD, verifying the PtRhSn niggliite structure.[24]

EOR evaluation results (Figure S25a in SI) manifested that both PtRh(Sn)/SnO_2 NPs and niggliite PtRhSn/C NPs exhibited higher activity than commercial Pt black at 0.5 V. In particular, the current density of PtRhSn/C NPs at 0.5 V (0.082 mA·cm^{-2}) was 8 times as much as that of Pt black, and

DOI: 10.1021/cs5018419
ACS Catal. 2015, 5, 1995−2008

the onset potential of the LSV curve shifted 0.15 V to low potential as compared with that of Pt black. In contrast with the three most active shaped Pt−Pd−Rh nanocrystals (i.e., PtPdRh NTOs, Pt_3PdRh NTO, and 8.8 nm PtPdRh NCs-200), niggliite PtRhSn/C NPs had its advantages at low potential toward EOR undoubtedly. The intersection point of the LSV curve of PtRhSn/C NPs with those of the three Pt−Pd−Rh nanocatalysts was around 0.53 V versus NHE, implying that the specific activity of the best Pt−Pd−Rh nanocatalysts surpassed that of niggliite PtRhSn/C NPs above 0.53 V. The chronoamperometric experiment at 0.5 V (Figure S25b and Table S8 in SI) showed that the durability of niggliite PtRhSn/C NPs was better than that of Pt−Pd−Rh NTOs but worse than that of 8.8 and 13.8 nm Pt−Pd−Rh NCs-200.

In a word, the EOR activity of the optimal Pt−Pd−Rh nanocatalysts obtained in this work was comparative to that of niggliite PtRhSn/C NPs near 0.5 V versus NHE, and a better durability was observed for the Pt−Pd−Rh NCs-200. There was much in common for the Pt−Pd−Rh and Pt−Rh−Sn trimetallic EOR nanocatalysts. Judging from the starting point for the design of the multicomponent EOR catalysts, both Pd and Sn were proposed to be the site to provide the oxidation reaction with sufficient oxidants at low potential. Acting as the site to facilitate the oxidation, Sn was a better candidate than Pd according to the large oxidation peak of Pt−Rh−Sn NPs at low potential. Several Pt−Pd−Rh NPs (e.g., PtPdRh NTOs, $PtPd_3Rh$ NTOs) suffered from the slow CO oxidation kinetics. However, the incorporation of Pd into PtRh-based NPs was proved to be a valid method to promote the cleavage of the C−C bond and elevate the selectivity to CO_2, especially by the construction of (111) facets. For Pt−Rh−Sn NPs, many groups stated that Sn component contributed little to the breakdown of the C−C bond in EOR.[17,27,70] Recently, Teng's group manifested the promoted selectivity in Pt-SnO_2 NPs by constructing a core−shell NPs.[65] Hence, the comparable activity of Pt−Pd−Rh NPs should benefit from the enhanced capability on the breakdown of the C−C bond with the introduction of Pd. Boosting the CO oxidation kinetics could probably enhance the reactivity of Pt−Pd−Rh NPs for the exploration of high efficient multicomponent EOR nanocatalysts.

4. CONCLUSIONS

In this work, composition-varied (100)-terminated Pt−Pd−Rh NCs and (111)-terminated Pt−Pd−Rh NTOs were prepared in a facile hydrothermal method by controlling the reduction tendency of the three metal precursors with the help of halides. Pt−Pd−Rh NTOs had atomic-level alloyed surface element distribution, whereas more Rh was segregated on the Rh-enriched surface of Pt−Pd−Rh NCs. A synergistic effect among Pt, Pd, and Rh toward EOR was revealed, with the combination of DFT calculations and experiments. It was demonstrated that Pd in the Pt−Pd−Rh nanocrystals contributed to the promoted activity and durability by offering oxidative hydroxyl groups to facilitate the oxidation of adsorbed species as well as modulating the electronic structure. Pt_3PdRh NTOs, PtPdRh NTOs, and 8.8 nm PtPdRh NCs-200 with homogeneous element distribution were found to show the most enhanced EOR activity at 0.5 V vs NHE, 5 times as much as that of commercial Pt black. It is worthwhile to note that 8.8 nm PtPdRh NCs-200 exhibited the highest activity even after 1 h in the chronoamperometric experiments under 0.5 V. Element distribution, morphology, particle size, and composition were revealed to affect the EOR performance of Pt−Pd−Rh nanocrystals. Among these factors, the influences of particle size, element distribution, and overall composition were attributed to the alteration of surface composition. In other words, surface composition was able to be tuned by controlling the overall composition, particle size, and element distribution. Hence, shape and surface compositions were considered as the original factors to the EOR reactivity.

According to the mechanism study by in situ FTIR, a prominent selectivity to CO_2 was observed on both Pt−Pd−Rh NTOs and Pt−Pd−Rh NCs-200, indicating that their promoted activity resulted from the strong capability in breakdown of C−C bond. In particular, (111)-terminated PtPdRh NTOs hold the ability to fully oxidize ethanol to CO_2 at extremely low potential (0.35 vs NHE) and the highest selectivity to CO_2 among all the measured catalysts. Integrated with DFT calculation and mechanism study, the key factors to affect the EOR activity over Pt−Pd−Rh nanocrystals were deduced as morphology and surface composition. It was proved that optimal Pt−Pd−Rh nanocatalysts toward EOR could simply be screened with DFT calculations of two elementary reactions (i.e., breakdown of C−C bond and oxidation of CO_{ad}). The results not only demonstrated a robust way to promote EOR performance by modulating surface structure and composition of the ternary metallic nanocatalysts but also provided an example for the rational construction of efficient nanocatalysts with the integrated multiple active components on tunable surfaces in high complexity for complicated heterogeneous reactions.

■ ASSOCIATED CONTENT

Supporting Information

The following file is available free of charge on the ACS Publications website at DOI: 10.1021/cs5018419.

PXRD patterns, EXAFS spectra, more TEM images and catalytic properties, and other data (PDF)

■ AUTHOR INFORMATION

Corresponding Authors

*E-mail: ywzhang@pku.edu.cn.
*E-mail: zhouzy@xmu.edu.cn.
*E-mail: yan@pku.edu.cn.

Author Contributions

‡W.Z. and J.K. contributed equally.

Notes

The authors declare no competing financial interest.

■ ACKNOWLEDGMENTS

This work was supported by the National Science Foundation of China (NSFC) (Grant Nos. 21025101, 21271011, 21173008, and 21321001). Y.W.Z. particularly appreciates the financial aid of China National Funds for Distinguished Young Scientists from the NSFC. R.S. acknowledges the support from the Hundred Talents project of the Chinese Academy of Sciences. We also highly appreciate the reviewers' constructive suggestions.

■ REFERENCES

(1) Hunber, G. W.; Iborra, S.; Corma, A. *Chem. Rev.* **2006**, *106*, 4044−4098.
(2) Agarwal, A. K. *Prog. Energy Combust.* **2007**, *33*, 233−271.

DOI: 10.1021/cs5018419
ACS Catal. 2015, 5, 1995−2008

(3) Goettemoeller, J.; Goettemoeller, A. *Sustainable Ethanol: Biofuels, Cellulosic Biomass, Flex-fuel Vehicles, and Sustainable Farming for Energy Independence*; Prairie Oak Publishing: Maryville, MO, 2007.
(4) Wang, J. T.; Savinell, R. F. *J. Electrochem. Soc.* **1995**, *142*, 4218−4224.
(5) Vielstich, W.; Lamm, A.; Gasteiger, H. A. *Handbook of Fuel Cells: Fundamentals, Technology, Applications*; Wiley: Chichester, U.K., 2003.
(6) Antolini, E.; Gonzalez, E. *J. Power Sources* **2010**, *195*, 3431−3450.
(7) Kamarudin, M.; Kamarudin, S.; Masdar, M.; Daud, W. *Int. J. Hydrogen Energy* **2013**, *38*, 9438−9453.
(8) Xia, X. H.; Liess, H.-D.; Twasita, T. *J. Electroanal. Chem.* **1997**, *437*, 233−240.
(9) Vigier, F.; Rousseau, S.; Coutanceau, C.; Leger, J.-M.; Lamy, C. *Top. Catal.* **2006**, *40*, 111−121.
(10) Wang, H.; Jusys, Z.; Behm, R. *J. Power Sources* **2006**, *154*, 351−359.
(11) Schmidt, V.; Ianniello, R.; Pastor, E.; González, S. *J. Phys. Chem.* **1996**, *100*, 17901−17908.
(12) Kutz, R.; Braunschweig, B.; Mukherjee, P.; Behrens, R.; Dlott, D.; Wieckowski, A. *J. Catal.* **2011**, *278*, 181−188.
(13) Vigier, F.; Coutanceau, C.; Hahn, F.; Belgsir, E.; Lamy, C. *J. Electroanal. Chem.* **2004**, *563*, 81−89.
(14) Méndez, E.; Rodríguez, J.; Arévalo, M.; Pastor, E. *Langmuir* **2002**, *18*, 763−772.
(15) Cantane, D.; Ambrosio, W.; Chatenet, M.; Lima, F. *J. Electroanal. Chem.* **2012**, *681*, 56−65.
(16) Souza, J.; Queiroz, S.; Bergamaski, K.; Gonzalez, E.; Nart, F. *J. Phys. Chem. B* **2002**, *106*, 9825−9830.
(17) Kowal, A.; Li, M.; Shao, M.; Sasaki, K.; Vukmirovic, M.; Zhang, J.; Marinkovic, N.; Liu, P.; Frenkel, A.; Adzic, R. *Nat. Mater.* **2009**, *8*, 325−330.
(18) Li, M.; Zhou, W. P.; Marinkovic, N.; Sasaki, K.; Adzic, R. *Electrochim. Acta* **2013**, *104*, 454−461.
(19) Li, M.; Cullen, D. A.; Sasaki, K.; Marinkovic, N. S.; More, K.; Adzic, R. R. *J. Am. Chem. Soc.* **2013**, *135*, 132−141.
(20) Zhou, W. J.; Zhou, Z. H.; Song, S. Q.; Li, W. Z.; Sun, G. Q.; Tsiakaras, P.; Xin, Q. *Appl. Catal., B* **2003**, *46*, 273−285.
(21) Tanaka, S.; Umeda, M.; Ojima, H.; Usui, Y.; Kimura, O.; Uchida, I. *J. Power Sources* **2005**, *152*, 34−39.
(22) Song, S. Q.; Tsiakaras, P. *Appl. Catal., B* **2006**, *63*, 187−193.
(23) Zhou, W. J.; Li, W. Z.; Song, S. Q.; Zhou, Z. H.; Jiang, L. H.; Sun, G. Q.; Xin, Q.; Poulianitis, K.; Kontou, S.; Tsiakaras, P. *J. Power Sources* **2004**, *131*, 217−223.
(24) Beyhan, S.; Coutanceau, C.; Léger, J.-M.; Napporn, T. W.; Kadırgan, F. *Int. J. Hydrogen Energy* **2013**, *38*, 6830−6841.
(25) Beyhan, S.; Léger, J.-M.; Kadırgan, F. *J. Power Sources* **2013**, *242*, 503−509.
(26) Beyhan, S.; Coutanceau, C.; Léger, J.-M.; Napporn, T. W.; Kadırgan, F. *Appl. Surf. Sci.* **2014**, *321*, 426−431.
(27) Beyhan, S.; Léger, J.-M.; Kadırgan, F. *Appl. Catal., B* **2014**, *144*, 66−74.
(28) Erini, N.; Loukrakpam, R.; Petkov, V.; Baranova, E.; Yang, R. Z.; Teschner, D.; Huang, Y. H.; Brankovic, S.; Strasser, P. *ACS Catal.* **2014**, 1859−1867.
(29) Babu, P.; Kim, H.; Chung, J.; Oldfield, E.; Wieckowski, A. *J. Phys. Chem. B* **2004**, *108*, 20228−20232.
(30) Wang, L.; Yamauchi, Y. *Chem. Mater.* **2011**, *23*, 2457−2465.
(31) Zhang, G.-R.; Wu, J.; Xu, B.-Q. *J. Phys. Chem. C* **2012**, *116*, 20839−20847.
(32) Zhu, H. Y.; Zhang, S.; Guo, S. J.; Su, D.; Sun, S. H. *J. Am. Chem. Soc.* **2013**, *135*, 7130−7133.
(33) Wu, Y. E.; Wang, D. S.; Chen, X. B.; Zhou, G.; Yu, R.; Li, Y. D. *J. Am. Chem. Soc.* **2013**, *135*, 12220−12223.
(34) Strasser, P.; Koh, S.; Anniyev, T.; Greeley, J.; More, K.; Yu, C.; Liu, Z.; Kaya, S.; Nordlund, D.; Ogasawara, H.; Toney, M. F.; Nilsson, A. *Nat. Chem.* **2010**, *2*, 454−460.
(35) An, K.; Alayoglu, S.; Ewers, T.; Somorjai, G. A. *J. Colloid Interface Sci.* **2012**, *373*, 1−13.
(36) Gu, J.; Zhang, Y.-W.; Tao, F. *Chem. Soc. Rev.* **2012**, *41*, 8050−8065.
(37) Zhou, K. B.; Li, Y. D. *Angew. Chem., Int. Ed.* **2012**, *51*, 602−613.
(38) Wang, D.-Y.; Chou, H.-L.; Lin, Y.-C.; Lai, F.-J.; Chen, C.-H.; Lee, J.-F.; Hwang, B.-J.; Chen, C.-C. *J. Am. Chem. Soc.* **2012**, *134*, 10011−10020.
(39) Strasser, P.; Fan, Q.; Devenney, M.; Weinberg, W.; Liu, P.; Nørskov, J. *J. Phys. Chem. B* **2003**, *107*, 11013−11021.
(40) Nilekar, A. U.; Alayoglu, S.; Eichhorn, B.; Mavrikakis, M. *J. Am. Chem. Soc.* **2010**, *132*, 7418−7428.
(41) Choi, Y.; Liu, P. *Catal. Today* **2011**, *165*, 64−70.
(42) Yin, A.-X.; Min, X.-Q.; Zhang, Y.-W.; Yan, C.-H. *J. Am. Chem. Soc.* **2011**, *133*, 3816−3819.
(43) Aliaga, C.; Park, J.; Yamada, Y.; Lee, H.; Tsung, C.-K.; Yang, P.; Somorjai, G. *J. Phys. Chem. C* **2009**, *113*, 6150−6155.
(44) Trasatti, S.; Petrii, O. *Pure Appl. Chem.* **1991**, *63*, 711−734.
(45) Miyake, H.; Okada, T.; Samjeske, G.; Osawa, M. *Phys. Chem. Chem. Phys.* **2008**, *10*, 3662.
(46) Sun, S.-G.; Yang, D.-F.; Tian, Z.-W. *J. Electroanal. Chem.* **1990**, *289*, 177−187.
(47) Zhang, Y.; Grass, M. E.; Kuhn, J. N.; Tao, F.; Habas, S. E.; Huang, W.; Yang, P.; Somorjai, G. A. *J. Am. Chem. Soc.* **2008**, *130*, 5868−5869.
(48) Wang, S.-B.; Zhu, W.; Ke, J.; Lin, M.; Zhang, Y.-W. *ACS Catal.* **2014**, *4*, 2298−2306.
(49) Huang, X.; Zhang, H.; Guo, C.; Zhou, Z.; Zheng, N. *Angew. Chem., Int. Ed.* **2009**, *48*, 4808−4812.
(50) Huang, X.; Li, Y.; Li, Y.; Zhou, H.; Duan, X.; Huang, Y. *Nano Lett.* **2012**, *12*, 4265−4270.
(51) Kavanagh, R.; Cao, X.-M.; Lin, W.-F.; Hardacre, C.; Hu, P. *Angew. Chem., Int. Ed.* **2012**, *51*, 1572−1575.
(52) Oliveira, R. T. S.; Santos, M. C.; Marcussi, B. G.; Tanimoto, S. T.; Bulhões, L. O. S.; Pereira, E. .C. *J. Power Sources* **2006**, *157*, 212−216.
(53) Dean, J. A. *Lange's Handbook of Chemistry*, 15th ed.; McGraw-Hill Professional: New York, 1998; Section 8, pp 132−133.
(54) Rand, D. A. J.; Woods, R. *J. Electroanal. Chem.* **1972**, *36*, 57−69.
(55) Topalov, A.; Cherevko, S.; Zeradjanin, A.; Meier, J.; Katsounaros, I.; Mayrhofer, K. *Chem. Sci.* **2013**, *5*, 631−638.
(56) Brodsky, C. N.; Young, A. P.; Ng, K. C.; Kuo, C.-H.; Tsung, C.-K *ACS Nano* **2014**, *8*, 9368−9378.
(57) Gómez, R.; Orts, J. M.; Feliu, J. M.; Clavilier, J.; Klein, L. H. *J. Electroanal. Chem.* **1997**, *432*, 1−5.
(58) Marković, N. M.; Ross, P. N. *Surf. Sci. Rep.* **2002**, *45*, 121−229.
(59) Yuan, Q.; Zhou, Z.; Zhuang, J.; Wang, X. *Chem. Mater.* **2010**, *22*, 2395−2402.
(60) Liu, Y.; Chi, M. F.; Mazumder, V.; Mor, K. L.; Soled, S.; Henao, J. D.; Sun, S. H. *Chem. Mater.* **2011**, *23*, 4199−4203.
(61) Hong, J. W.; Kim, D.; Lee, Y. W.; Kim, M.; Kang, S. W.; Han, S. W. *Angew. Chem., Int. Ed.* **2011**, *50*, 8876−8880.
(62) Clavilier, J.; Armand, D.; Sun, S. G.; Petit, M. *J. Electroanal. Chem.* **1986**, *205*, 267−277.
(63) Xiao, S.; Hu, W.; Luo, W.; Wu, Y.; Li, X.; Deng, H. *Eur. Phys. J. B* **2006**, *54*, 479−484.
(64) You, H.; Yang, S.; Ding, B.; Yang, H. *Chem. Soc. Rev.* **2013**, *42*, 2880−2904.
(65) Du, W.; Yang, G.; Wong, E.; Deskins, N. A.; Frenkel, A. I.; Su, D.; Teng, X. *J. Am. Chem. Soc.* **2014**, *136*, 10862−10865.
(66) Wang, Q.; Sun, G. Q.; Jiang, L. H.; Xin, Q.; Sun, S. G.; Jiang, Y. X.; Chen, S. P.; Jusys, Z.; Behm, R. *J. Phys. Chem. Chem. Phys.* **2007**, *9*, 2686−2696.
(67) Shao, M.; Adzic, R. *Electrochim. Acta* **2005**, *50*, 2415−2422.
(68) Lambert, D. K. *Electrochim. Acta* **1996**, *41*, 623−630.
(69) Li, M.; Kowal, A.; Sasaki, K.; Marinkovic, N.; Su, D.; Korach, E.; Liu, P.; Adzic, R. R. *Electrochim. Acta* **2010**, *55*, 4331−4338.
(70) Jiang, L.; Colmenares, L.; Jusys, Z.; Sun, G. Q.; Behm, R. J. *Electrochim. Acta* **2007**, *53*, 377−389.

DOI: 10.1021/cs5018419
ACS Catal. 2015, 5, 1995−2008